This article is a *Plant Cell* Advance Online Publication. The date of its first appearance online is the official date of publication. The article has been edited and the authors have corrected proofs, but minor changes could be made before the final version is published. Posting this version online reduces the time to publication by several weeks.

Single-Molecule Analysis of PIP2;1 Dynamics and Partitioning Reveals Multiple Modes of *Arabidopsis* Plasma Membrane Aquaporin Regulation [C][W]

Xiaojuan Li,[a,b,1] Xiaohua Wang,[a,b,1] Yong Yang,[c] Ruili Li,[a,b] Qihua He,[d] Xiaohong Fang,[c] Doan-Trung Luu,[e] Christophe Maurel,[e] and Jinxing Lin[a,2]

[a] Key Laboratory of Plant Molecular Physiology, Institute of Botany, Chinese Academy of Sciences, Beijing 100093, China
[b] Graduate University of Chinese Academy of Sciences, Beijing 100049, China
[c] Beijing National Laboratory for Molecular Sciences, Institute of Chemistry, Key Laboratory of Molecular Nanostructures and Nanotechnology, Chinese Academy of Sciences, Beijing 100190, China
[d] Peking University Health Science Center, Beijing 100191, China
[e] Biochimie et Physiologie Moléculaire des Plantes, Institut de Biologie Intégrative des Plantes, Unité Mixte de Recherche 5004 Centre National de la Recherche Scientifique/Unité Mixte de Recherche 0386 Institut National de la Recherche Agronomique/ Montpellier SupAgro/Université Montpellier 2, F-34060 Montpellier Cedex 2, France

PIP2;1 is an integral membrane protein that facilitates water transport across plasma membranes. To address the dynamics of *Arabidopsis thaliana* PIP2;1 at the single-molecule level as well as their role in PIP2;1 regulation, we tracked green fluorescent protein–PIP2;1 molecules by variable-angle evanescent wave microscopy and fluorescence correlation spectroscopy (FCS). Single-particle tracking analysis revealed that PIP2;1 presented four diffusion modes with large dispersion of diffusion coefficients, suggesting that partitioning and dynamics of PIP2;1 are heterogeneous and, more importantly, that PIP2;1 can move into or out of membrane microdomains. In response to salt stress, the diffusion coefficients and percentage of restricted diffusion increased, implying that PIP2;1 internalization was enhanced. This was further supported by the decrease in PIP2;1 density on plasma membranes by FCS. We additionally demonstrated that PIP2;1 internalization involves a combination of two pathways: a tyrphostin A23-sensitive clathrin-dependent pathway and a methyl-β-cyclodextrin–sensitive, membrane raft–associated pathway. The latter was efficiently stimulated under NaCl conditions. Taken together, our findings demonstrate that PIP2;1 molecules are heterogeneously distributed on the plasma membrane and that clathrin and membrane raft pathways cooperate to mediate the subcellular trafficking of PIP2;1, suggesting that the dynamic partitioning and recycling pathways might be involved in the multiple modes of regulating water permeability.

INTRODUCTION

Aquaporins, which facilitate the diffusion of water across biological membranes, are key molecules in the regulation of water transport at the cell and organ levels, and plasma membrane intrinsic proteins (PIPs) are the most abundant aquaporins in the plant plasma membrane (Katsuhara et al., 2008; Maurel et al., 2008). Plants have multiple PIP isoforms (13 in *Arabidopsis thaliana*), and on the basis of sequence similarity, PIPs can be divided into two groups, PIP1 and PIP2. PIPs are thought to occur as tetramers, with each subunit forming an individual aqueous pore, but recent work from several laboratories has indicated that PIP1s and PIP2s can assemble to form hetero-tetramers (Zelazny et al., 2007; Otto et al., 2010). The function of PIPs in plants has attracted extensive research. Certain PIP1s enhanced osmotic water transport upon expression in *Xenopus laevis* oocytes (Biela et al., 1999), and *Nicotiana tabacum* and *Arabidopsis* plants deficient in these or close PIP1 homologs showed reduced hydraulic conductivity in roots and shoots (Martre et al., 2002; Siefritz et al., 2002; Postaire et al., 2010). Yet, the water transport activity of other PIP1 homologs is still unclear (Fetter et al., 2004; Sommer et al., 2008), whereas all PIP2s examined so far have been shown to have high water channel activity (Fetter et al., 2004; Verdoucq et al., 2008), indicating that PIP2s play an important role in plant–water relations.

Many studies have also noted that the regulation properties of plant aquaporins can provide useful indications about their integrated function (Vera-Estrella et al., 2004; Chaumont et al., 2005; Boursiac et al., 2008; Maurel et al., 2008). In addition to regulated opening and closing (gating), plant aquaporins were shown to undergo highly controlled subcellular trafficking as a critical point for regulating their expression and function. In these respects, *Arabidopsis* PIP2;1 has emerged as a prototypic isoform. This aquaporin shows calcium- and proton-dependent

[1] These authors contributed equally to this work.
[2] Address correspondence to linjx@ibcas.ac.cn.
The author responsible for distribution of materials integral to the findings presented in this article in accordance with the policy described in the Instructions for Authors (www.plantcell.org) is: Jinxing Lin (linjx@ibcas.ac.cn).
[C]Some figures in this article are displayed in color online but in black and white in the print edition.
[W]Online version contains Web-only data.
www.plantcell.org/cgi/doi/10.1105/tpc.111.091454

gating upon reconstitution in proteoliposomes (Verdoucq et al., 2008). Its trafficking to the plasma membrane was shown to be dependent on a diacidic motif and ubiquitination (Lee et al., 2009; Sorieul et al., 2011). Studies on plant roots under salt stress also revealed a reactive oxygen species–dependent internalization of PIP2;1, which was linked to salt-induced changes in C-terminal phosphorylation (Boursiac et al., 2008; Prak et al., 2008). Several endocytic pathways for plasma membrane proteins have been identified in animal and plant cells, including clathrin-dependent and raft-associated pathways (Mayor and Pagano, 2007). The former pathway is constitutive and has been established for PIP2;1 and other plant membrane proteins (Dhonukshe et al., 2007). The latter is by far less understood in plants and may be triggered by specific signals (Mayor and Pagano, 2007). In this context, a critical issue is to understand how PIP2;1 responds to osmotic stress to regulate root hydraulic conductivity (*L*pr), particularly the initial events that determine PIP2;1 subcellular movements immediately after cell stimulation.

Although earlier studies focused on the structure and regulation mechanisms (Törnroth-Horsefield et al., 2006; Maurel et al., 2009), few have examined the diffusion dynamics and partitioning of membrane proteins in living cells, which is important for bridging data collected at the level of individual molecules to the physical and physiological processes (Joo et al., 2008). Bulk approaches have been unable to unambiguously determine the oligomeric state and mobility of molecules within living cells. Recent progress in single-molecule measurements has enabled observation of the dynamic behavior of membrane proteins and their elementary molecular processes (Dahan et al., 2003; Douglass and Vale, 2005; Zhang et al., 2009c; Hern et al., 2010). The aim of this study was to investigate the motion of PIP2;1 at a high spatiotemporal resolution in *Arabidopsis* cell membranes using variable-angle evanescent wave microscopy (EWM), also known as variable-angle epifluorescence microscopy, and fluorescence correlation spectroscopy (FCS) and to reveal heterogeneities or physical effects usually hidden in the ensemble average. Specifically, we focused on partitioning on the membrane and recycling pathways of PIP2;1 under resting and salt stress conditions.

RESULTS

The Assembly State of PIP2;1 in *Arabidopsis* Plasma Membranes

To monitor PIP2;1 molecules in plant plasma membranes and study their assembly state, it was necessary to label them specifically with a fluorescent species having suitable biophysical characteristics in terms of absorption wavelength and resistance to photobleaching. We performed fluorescence targeting experiments in *Arabidopsis* using green fluorescent protein (GFP) fusions. Although some fluorescent signals in transgenic lines driven by the native promoter could be detected by the electron-multiplying charge-coupled device (EMCCD) (see Supplemental Figure 1A and Supplemental Movie 1 online), the signals were weak and fluorescent spots could not be used for single-molecule analysis. Thus, we stably expressed the fusion

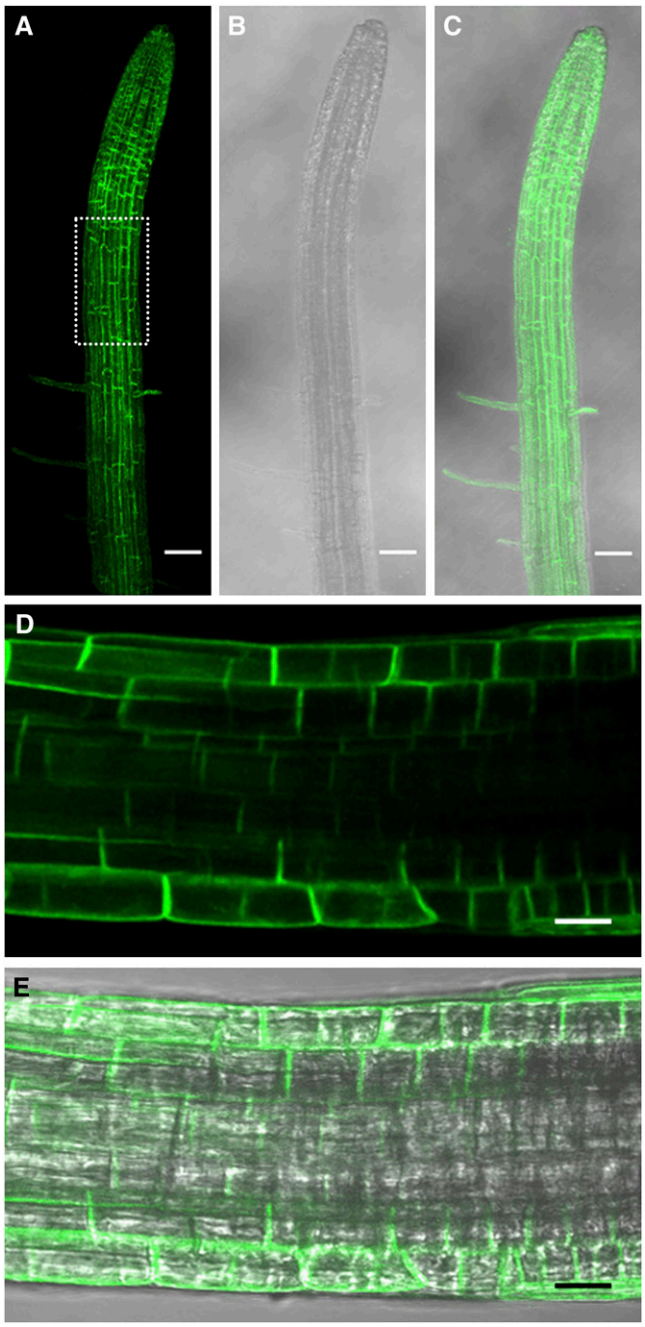

Figure 1. Confocal Microscopy Images of GFP-PIP2;1 Fusion Proteins Expressed in *Arabidopsis* Roots.

(A) to **(C)** Fluorescence, bright-field, and merged images showing that the GFP-PIP2;1 fusion protein could be efficiently expressed in *Arabidopsis* root cells, from the root apical meristem to the maturation zone. **(D)** and **(E)** Higher magnification of the area highlighted in **(A)**, showing extensive plasma membrane-restricted GFP fluorescence in the epidermis. Bars = 40 μm in **(A)** to **(C)** and 20 μm in **(D)** and **(E)**.

protein under control of the constitutive 35S promoter. Cells expressing GFP-labeled PIP2;1 (GFP-PIP2;1) were observed to ensure that the GFP insertion did not interfere with PIP2;1 plasma membrane targeting. Figure 1 shows that GFP-PIP2;1 was efficiently targeted to the plasma membrane of *Arabidopsis* root epidermal cells. Furthermore, the water transport activity of fluorescently tagged PIP2;1 was investigated after functional expression in *Xenopus* oocytes. Osmotic swelling assays showed that the osmotic water permeability (P_f) of oocytes injected with the GFP-PIP2;1 cRNAs was significantly higher (more than fivefold) than that of control oocytes expressing GFP alone.

When the plasma membrane of living root epidermal cells was viewed under EWM, numerous fluorescent spots were observed, most of which appeared as well-dispersed diffraction-limited fluorescent spots. Figure 2A shows a single video frame taken from a 45-s recording of the epidermal cell plasma membrane. To determine the number of GFP-PIP2;1 molecules contained in these diffraction-limited fluorescent spots, we performed calibration experiments using purified monomeric GFP, which was immobilized on cover glasses and visualized with EWM illumination. The brightness of a single GFP molecule could be detected in our measurement apparatus, and the fluorescence intensity distribution of diffraction-limited spots was analyzed. The background-corrected, area-integrated fluorescence intensities of individual spots produced a unimodal distribution with a peak intensity around 70 counts (see Supplemental Figure 1B online).

To investigate the oligomerization state of GFP-PIP2;1 in the plasma membrane of living cells, we analyzed the fluorescence intensity distribution of the GFP-PIP2;1 spots. A histogram of the intensity showed an asymmetric distribution skewed to intensities lower than that expected for four fluorophores (Figure 2B). The majority of spots had intensities ranging from 120 to 250 counts, which were approximately two- or threefold that of purified GFP, suggesting that these spots included two or three GFP-PIP2;1 molecules. To circumvent signal fluctuation due to the diffusion of GFP-PIP2;1 in living cell membranes, the photobleaching of individual spots was further analyzed in fixed cells. For each of the chosen fluorescent spots, we determined, as described previously (Ulbrich and Isacoff, 2007), the number of fluorescing GFP molecules by counting the number of bleaching steps. As shown in Figure 2C, the number of bleaching steps ranged from one to four for the analyzed puncta.

Molecular Behavior of GFP-PIP2;1 in the Plasma Membrane

We then studied the dynamic properties of PIP2;1 in more detail using single-particle tracking (SPT) in continuous images (Figures 3A and 3B; see Supplemental Movie 2 online). Some molecules covered relatively long distances (up to 0.767 μm within 100 ms), whereas others were less mobile (0.053 μm within 100 ms). The diffusion type was evaluated by analysis of mean square displacement (MSD) versus time plots of the trajectories of individual molecules (Figure 3C). The curve-fitting relationship between MSD and time showed that GFP-PIP2;1 diffusion could be classified into four categories: pure Brownian diffusion (33.75% ± 3.3% of the total trajectories; Figure 4A); directed diffusion (27.5% ± 2.4% of the total trajectories; Figure 4A); pure restricted or confined diffusion (17.5% ± 2.1% of the total trajectories; Figure 4A), with an average confinement range of 87.76% ± 9.4 nm; or diffusion with combinations of Brownian and restricted modes referred to as a mixed trajectory. The proportion of the last category was 21.25% ± 3.1% (Figure 4A), with the mean value of the confinement range (116.83 ± 10.7 nm) generally larger than that of pure restricted trajectories. Although one-third of the PIP2;1 spots had a pure Brownian diffusion, most PIP2;1 molecules were restricted in confinement zones, which were emphasized by the mixed trajectory regime.

The diffusion coefficient of the GFP-PIP2;1 particles was calculated by linear fit to MSD versus time (MSD-*t*) plots. The distribution of the diffusion coefficients was plotted in a histogram having logarithmically spaced bins (Figure 4B). The data were fitted using Gaussians, the position of the peak (noted as $\hat{G}$) being considered the characteristic diffusion coefficient. Figure 4B shows that $\hat{G}$ was around 2.46×10^{-3} $\mu m^2/s$ (SE 2.19 to 2.75×10^{-3} $\mu m^2/s$), with a large dispersion of diffusion coefficients, most of which were between 10^{-4} $\mu m^2/s$ and 3×10^{-2} $\mu m^2/s$, indicating that the movement of PIP2;1 was heterogeneous. When the diffusion coefficients and the percentage of different diffusion modes were plotted against the fluorescence intensity (a parameter that tends to reflect the level of GFP-PIP2;1 oligomerization) (see Supplemental Figures 2A and 2B online), we found that the diffusion characters were not directly associated with the fluorescence intensity.

We were curious as to whether the dynamic characteristics of GFP-PIP2;1 were general because no such analysis of membrane proteins has been reported in plant cells. Therefore, we compared the behavior of GFP-PIP2;1 and GFP-LTi6a, a small plasma membrane marker protein (see Supplemental Figures 3A and 3B online). As illustrated in Supplemental Figure 3C online, the diffusion coefficient of GFP-LTi6a ranged from 5.62×10^{-3} to 3.16×10^{-1} $\mu m^2/s$, with a $\hat{G}$ value of 2.37×10^{-2} $\mu m^2/s$ (SE 2.06 to 2.73×10^{-2} $\mu m^2/s$), which is 10-fold that of GFP-PIP2;1. To extract more information about the behavior of individual GFP-LTi6a fluorescent particles, we further analyzed the diffusion mode according to the initial selection criteria described above. Over 50% (51.27% ± 4.4%; see Supplemental Figure 3D online) of the GFP-LTi6a molecules exhibited Brownian diffusion, whereas other GFP-LTi6a molecules underwent directed diffusion and restricted diffusion (25.91% ± 3.9% and 21.53% ± 6.0%, respectively; see Supplemental Figure 3D online). However, almost no mixed trajectory was detected (only one among 77 trajectories). These results show that our analysis was sensitive enough to distinguish the dynamics of two different proteins. Thus, GFP-PIP2;1 exhibited specific dynamic properties.

Partitioning of PIP2;1 Is Associated with Membrane Rafts

To understand better the molecular mechanisms underlying PIP2;1 partitioning into plasma membrane domains, we treated seedlings with methyl-β-cyclodextrin (MβCD), a sterol disrupting reagent. The subsequent reduction in sterol levels was monitored by cell staining with filipin, a fluorescent polyene antibiotic that binds to sterols. Treatment with 10 mM MβCD resulted in the effective depletion of sterol in root cells by ~30% (see

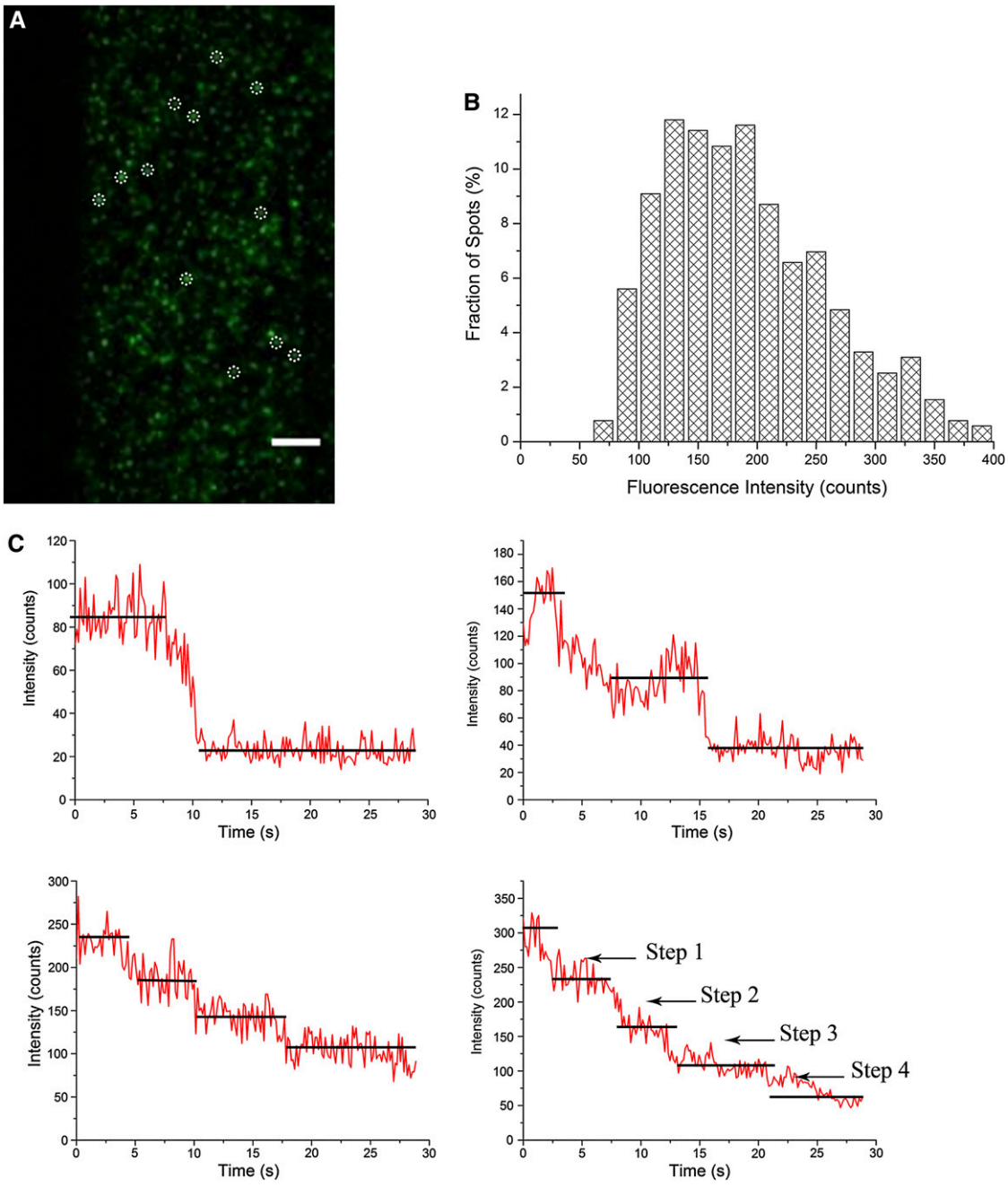

Figure 2. GFP-PIP2;1 Molecules on the Plasma Membrane of Root Epidermal Cells Imaged with EWM and Oligomeric State Analysis.

(A) A typical single-molecule image of GFP-PIP2;1 on the plasma membrane of living epidermal cells. The image is a section of the first frame of a stack of images with the background subtracted. The diffraction-limited spots (3 × 3 pixel regions) enclosed within white circles represent the signals from individual GFP-PIP2;1 fluorescent spots and were chosen for the fluorescence intensity analysis. Bar = 5 μm.
(B) Distribution of the fluorescence intensity of diffraction-limited GFP-PIP2;1 spots from the living cell imaging (*n* = 523 spots).
(C) Time courses of GFP emission after background correction showing one-step, two-step, three-step, and four-step bleaching. The amplitude of each step was close to that of single purified GFP molecules observed on cover slips (see Supplemental Figure 1 online).
[See online article for color version of this figure.]

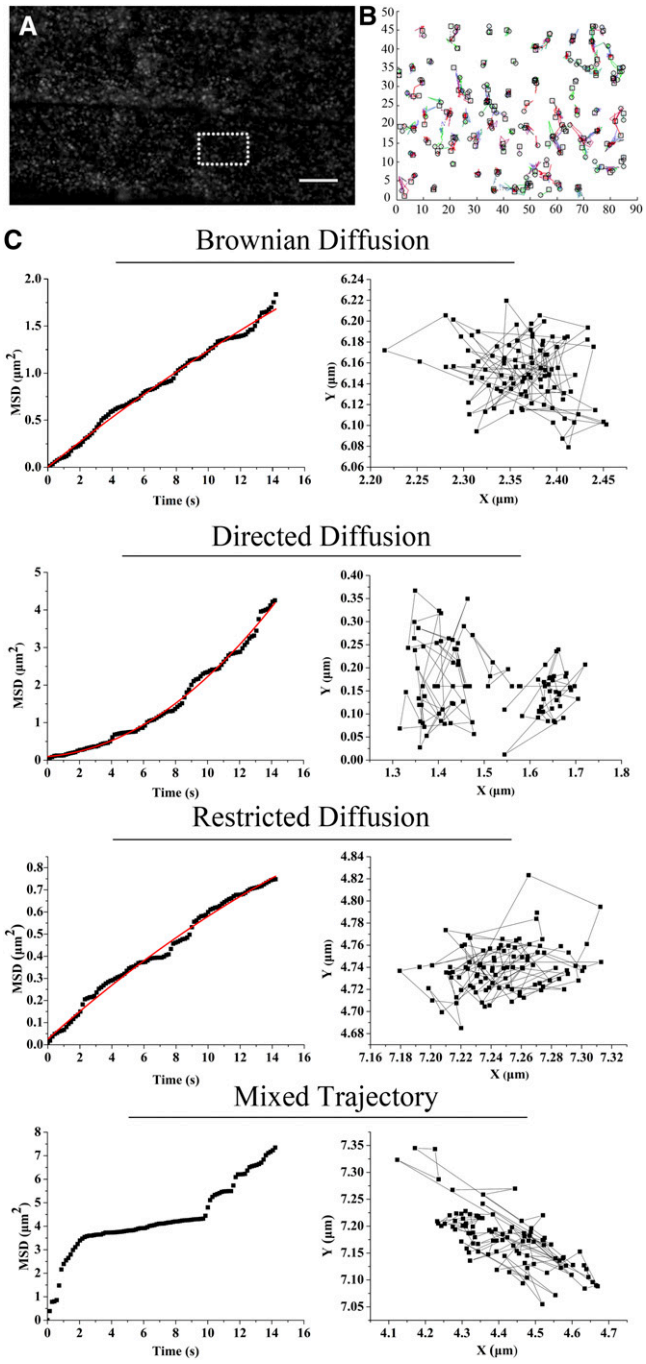

Figure 3. Automated Tracking and Statistical Analysis of GFP-PIP2;1 Spots on the Plasma Membrane.

(A) EWM image of GFP-PIP2;1 on the plasma membrane of epidermal cells. Bar = 10 μm.

(B) Trajectories of GFP-PIP2;1 molecules in the area indicated by the white box in **(A)**. The indicated trajectories result from automated tracking of individual puncta in a series of stacks.

(C) Analysis by MSD of various trajectories and classification into different diffusion modes. The resulting MSD-*t* curves (black squares) were fitted with pure Brownian, restricted, directed, and those exhibiting a combination of Brownian and restricted modes were regarded as mixed trajectories. A representative sample of the various diffusion modes of GFP-PIP2;1 on the plasma membrane is shown with the corresponding trajectories. Note that classification into various diffusion modes could not have been accurately performed using simple visual inspection of the trajectories.

[See online article for color version of this figure.]

Supplemental Figure 4 online). Under confocal laser scanning microscopy and EWM, we found that actin filaments became slightly shorter after treatment with MβCD, whereas the elongation rate and the rate of convolution frequency did not significantly change (see Supplemental Figure 5, Supplemental Movies 3 and 4, and Supplemental Table 1 online), suggesting that MβCD treatment did not significantly affect the organization of the actin cytoskeleton. As shown in Figure 5B, treatment with MβCD induced dramatic changes in the partitioning of GFP-PIP2;1 in the plasma membrane compared with that in control cells (Figure 5A). More specifically, the well dispersed patterns of diffraction-limited spots disappeared. Instead, some particles accumulated into small clusters, which were brighter than diffraction-limited spots (purple circles in Figure 5B). Disappearance of PIP2;1 molecules in certain areas was also observed. We further followed the impacts of fenpropimorph (Fen), a sterol synthesis inhibitor, and DL-threo-1-phenyl-2-palmitoylamino-3-morpholino-1-propanol (PPMP), a sphingolipid biosynthesis inhibitor, on the localization of GFP-PIP2;1. Both inhibitors resulted in GFP-PIP2;1 coalescing into larger particles with an increased fluorescence intensity (see Supplemental Figure 6 online), similar to the effect of MβCD treatment. These results suggest that the partitioning of PIP2;1 in the plasma membrane depends on membrane lipids and on the sterol content.

Because of its multiple diffusion modes and dependency on sterol, we suspected that PIP2;1 localized at least partially to sphingolipid-rich microdomains referred to as membrane rafts (Bhat and Panstruga, 2005). To validate this assumption, cells coexpressing GFP-PIP2;1 and mCherry-Flotillin1 (At-Flot1, a marker protein of membrane rafts) were imaged by dual-color EWM. Excitation was switched between two lasers so that the cells were alternatively illuminated with blue (473 nm) and green (561 nm) light, and sequential video frames were obtained. When two consecutive frames representing green and red fluorescence were overlaid, we detected some yellow regions caused by the high intensity in both the green and red channels, suggesting an overlap of the GFP-PIP2;1 and mCherry-Flot1 fluorescent foci. An example of colocalization is shown in Figures 5C to 5E, and the lateral diffusion trajectories of the overlapped fluorescent spots are shown in Figures 5F and 5G. To test the possibility that the colocalization was due to random overlap of the highly dense foci on the cell membrane, the red channel image from four different cells was rotated 180° with respect to the green channel, as reported in a previous investigation (Konopka et al., 2008). The average peak distance for the original image (4.27 ± 1.38 pixels; n = 211 from four cells) was significantly smaller from that of the rotated images (6.82 ± 2.18 pixels;

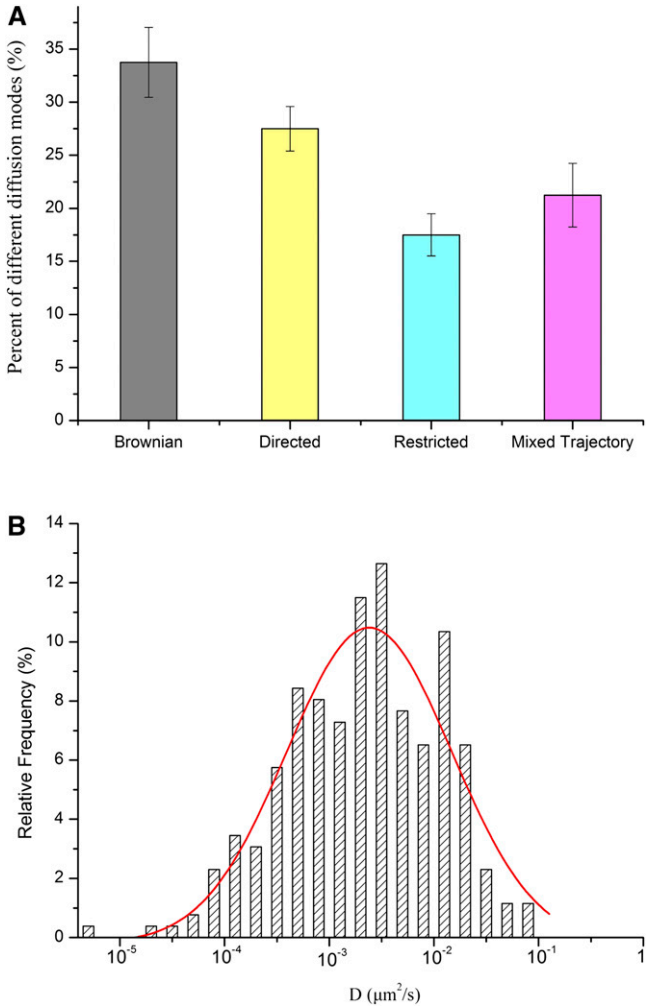

Figure 4. Statistical Analyses of GFP-PIP2;1 Lateral Dynamics on the Plasma Membrane.

(A) Relative percentage of the different diffusion modes of GFP-PIP2;1 derived from three separate analysis of a total $n = 80$ individual trajectories. Values given are mean ± SD.

(B) Distribution of diffusion coefficients (D) for GFP-PIP2;1 on the plasma membrane of epidermal cells ($n = 261$ spots).

[See online article for color version of this figure.]

$n = 213$ from four cells, $P < 0.0001$), indicating that the colocalization was significant.

Tracking the fluorescent spots of GFP-PIP2;1 from their colocalization with mCherry-Flot1 clearly showed that the movements of these GFP-PIP2;1 spots were mainly confined within a specific area, the average displacement of the confined GFP-PIP2;1 being 88.87 ± 8.2 nm (mean ± SE; $n = 21$). These spots also exhibited restricted or mixed trajectory diffusion (Figures 5F and 5G). Within the mixed trajectories, GFP-PIP2;1 exhibited restricted diffusion when it was confined in mCherry-Flot1–rich structures. These results imply that the partitioning of PIP2;1 on membranes is closely related to membrane rafts.

Salt Exposure Triggers Relocalization and Dynamic Changes

The effects of treating roots with 100 mM NaCl on GFP-PIP2;1 cellular dynamics were first investigated using confocal laser scanning microscopy. Whereas homogenous labeling of the plasma membrane by GFP-PIP2;1 was observed under normal conditions (Figure 1D), salt exposure resulted in a discontinuous labeling pattern after 10 min (Figures 6A and 6B); a similar phenomenon was also detected using 200 mM sorbitol as a comparable osmotic stress (see Supplemental Figure 7A online). After staining with FM4-64, a plasma membrane marker, the plasma membrane areas with discontinuous GFP labeling were found to be intact and unperturbed by the salt treatment (Figure 6C). Furthermore, we observed the appearance of intracellular structures containing GFP-PIP2;1 in a restricted number of cells (Figure 6D). Parallel experiments with seedlings expressing GFP-LTi6a, an independent marker of the plasma membrane, showed much less pronounced relocalization of GFP-LTi6a after NaCl and sorbitol treatments (see Supplemental Figures 7B to 7D online).

When observed by EWM, salt-treated epidermal cells displayed highly mobile puncta dispersed on the membrane (Figure 6E; see Supplemental Movie 5 online). The dynamic characteristics of GFP-PIP2;1 after treatment with 100 mM NaCl were also investigated using SPT analysis. As illustrated in the histogram of Figure 6F, the diffusion coefficients of GFP-PIP2;1 in NaCl-treated cells ranged mainly from 10^{-3} to 10^{-1} $\mu m^2/s$ (1×10^{-4} to 3×10^{-2} $\mu m^2/s$ in control cells); the highest value of 1.94×10^{-1} $\mu m^2/s$ was 2 times higher than in control cells (9.8×10^{-2} $\mu m^2/s$). More specifically, $\hat{G}$ increased to 5.62×10^{-3} $\mu m^2/s$ (SE 4.57 to 6.92 $\times$ 10^{-3} $\mu m^2/s$), more than twofold that of the diffusion coefficient of PIP2;1 in control cells (2.5×10^{-3} $\mu m^2/s$). To investigate further the behavior of PIP2;1 in living cells exposed to salt, the percentage of different diffusion modes was also analyzed. As shown in Figure 6G, and with respect to normal conditions, Brownian diffusion, directed diffusion, and mixed trajectory decreased to 83.33, 91, and 88% of the control values, respectively, while restricted diffusion increased significantly to 160% compared with control cells (Figure 6G). These changes indicate that in relation to the modified surface and intracellular GFP-PIP2;1 labeling observed under NaCl treatment conditions, diffusion coefficients were skewed toward higher values and more GFP-PIP2;1 molecules underwent restricted diffusion.

Membrane Rafts and Clathrin Contribute to the Internalization of PIP2;1

Endocytosis is a basic cellular process used by cells to internalize a variety of molecules (Robinson et al., 2008). The discovery of clathrin-dependent endocytosis has provided a fundamental paradigm for analyzing membrane trafficking in cells (Dhonukshe et al., 2007; Pérez-Gómez and Moore, 2007; Foresti et al., 2010). Moreover, a sterol-dependent pathway has also been reported to play an important role in *Arabidopsis* (Men et al., 2008). To investigate the pathways that are involved in PIP2;1 trafficking under normal conditions and in its relocalization upon stimulation, we compared the localization of PIP2;1 to that of clathrin

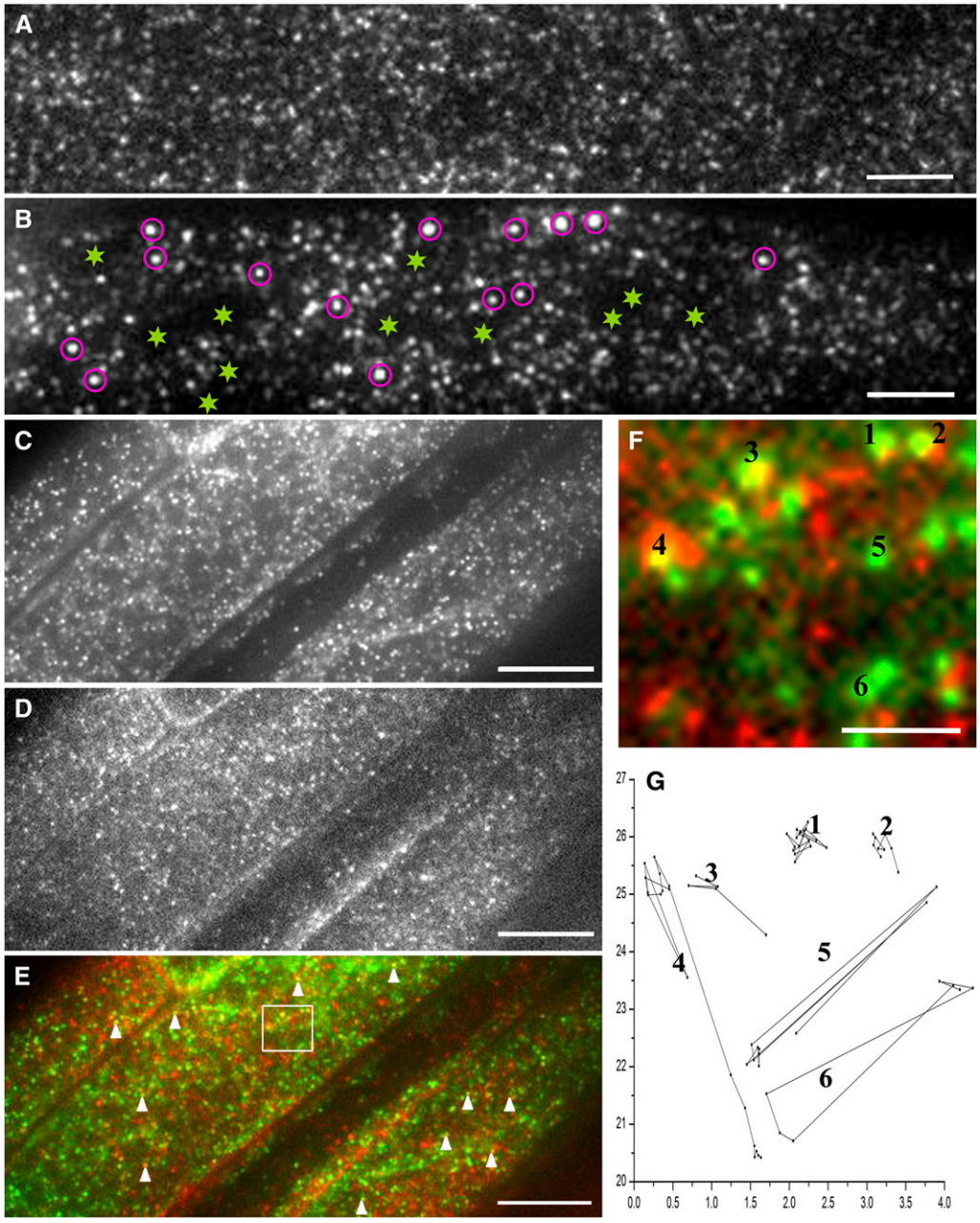

Figure 5. The Partitioning of GFP-PIP2;1 on the Plasma Membrane Is Associated with Membrane Rafts.

(A) The partitioning of GFP-PIP2;1 on the plasma membrane of epidermal cells bathed in half-strength MS medium.
(B) Effects of sterol depletion induced by a MβCD treatment on the plasma membrane partitioning of GFP-PIP2;1. Some GFP-PIP2;1 molecules assembled into small clusters (indicated in purple circles) to yield dots that were larger and brighter than diffraction-limited spots. Disappearance of PIP2;1 molecules in certain areas was also observed, as highlighted with asterisks.
(C) to **(E)** The first frame from a dual-color EWM movie of GFP-PIP2;1 **(C)**/mCherry-Flot1 **(D)**/merged images **(E)** of the same epidermal cells bathed in half-strength MS medium. Arrowheads indicate the colocalization fluorescent foci.
(F) Higher magnification of the boxed area in **(E)**.
(G) Lateral diffusion trajectories of the corresponding GFP-PIP2;1 signal in **(F)**. Movements of spots 1 to 3 colocalized with mCherry-Flot1 and were confined to certain areas, while spot 4 covered a larger range after a transient trapping. Nonoverlapped spots 5 and 6 covered a longer range compared with spots 1 and 2.
Bars = 5 μm in **(A)** and **(B)**, 10 μm in **(C)** to **(E)**, and 2 μm in **(F)**.

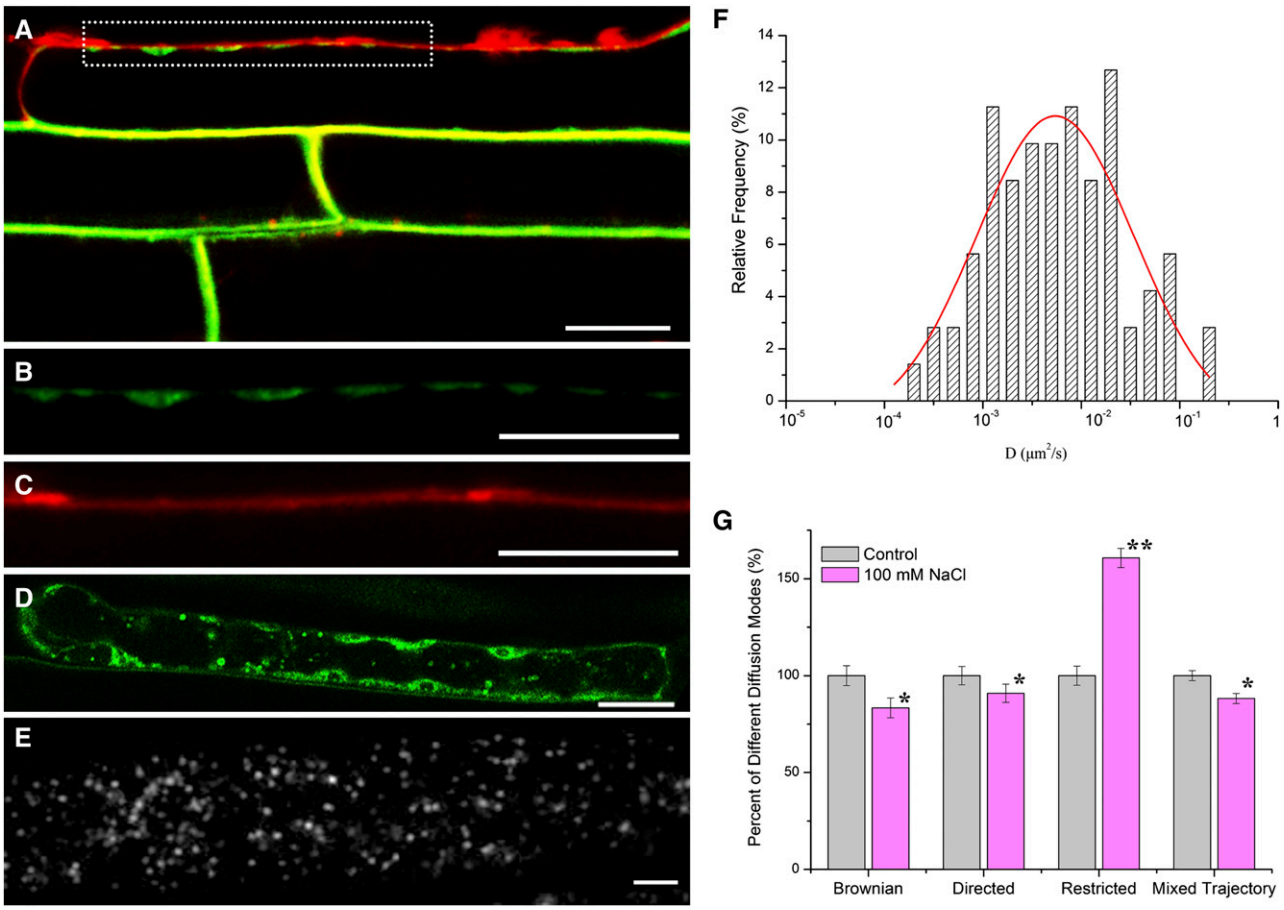

Figure 6. Confocal Images and EWM Analysis of GFP-PIP2;1 after NaCl Treatment.

(A) The plasma membrane of an epidermal cell from GFP-PIP2;1 seedlings stained with FM4-64 after treatment with NaCl.
(B) Detail of the plasma membrane indicated discontinuous labeling by GFP-PIP2;1, as highlighted by the white box in **(A)**.
(C) Corresponding FM4-64 staining of the plasma membrane to **(B)** indicates that the membrane was intact and unperturbed.
(D) Labeling of intracellular structures by GFP-PIP2;1.
(E) EWM image of NaCl-treated epidermal cells.
(F) Histogram showing the distribution of diffusion coefficients of GFP-PIP2;1 in NaCl-treated epidermal cells (n = 171 spots).
(G) Percentage of different diffusion modes in NaCl-treated cell (n = 80 individual trajectories) compared with those in control cells bathed in half-strength MS medium. Values given are mean ± SD. **Significantly different from the control at $P < 0.01$; *significantly different from the control at $P < 0.05$, t test. Bars = 20 μm in **(A)** to **(D)** and 5 μm in **(E)**.

light chain (CLC) and Flot1, two commonly used endocytic markers for the clathrin-dependent pathway and membrane raft–associated pathway, respectively. Cells coexpressing GFP-PIP2;1/mCherry-Flot1 or GFP-PIP2;1/mCherry-CLC were imaged using dual-color EWM. Instead of diffraction-limited fluorescent foci with lateral diffusion on the membranes, we detected green and red particles or clusters that were localized in the cytoplasm region proximal to the plasma membrane and that exhibited movements of departing from membranes. For quantification, two particles were arbitrarily considered as codiffusing when at least one pixel of their fluorescence signals overlapped during at least five consecutive frames acquired within a 200-ms interval. As illustrated in Figure 7, GFP-PIP2;1 was found to colocalize with mCherry-CLC and gradually codiffused away from the focus, indicating that the internalization of PIP2;1 was associated with the clathrin-dependent pathway. As shown in Figure 8, partial colocalization and codiffusion of GFP-PIP2;1 and mCherry-Flot1 were also detected, suggesting that, under normal conditions, the internalization of PIP2;1 was also associated with membrane rafts but to a lesser extent than with clathrin.

To understand at a quantitative level how both recycling pathways contribute to GFP-PIP2;1 internalization, we examined the temporal interactions using live-cell fluorescence cross-correlation spectroscopy (FCCS). The fluorescence fluctuation of GFP and mCherry gave rise to cross-correlation signals in both seedlings expressing GFP-PIP2;1/mCherry-CLC or GFP-PIP2;1/mCherry-Flot. The relative cross-correlation amplitude was 0.53 ± 0.11 for GFP-PIP2;1/mCherry-CLC, while the value was 0.42 ± 0.13 for GFP-PIP2;1/mCherry-Flot1, suggesting that the interaction between GFP-PIP2;1 and mCherry-CLC was

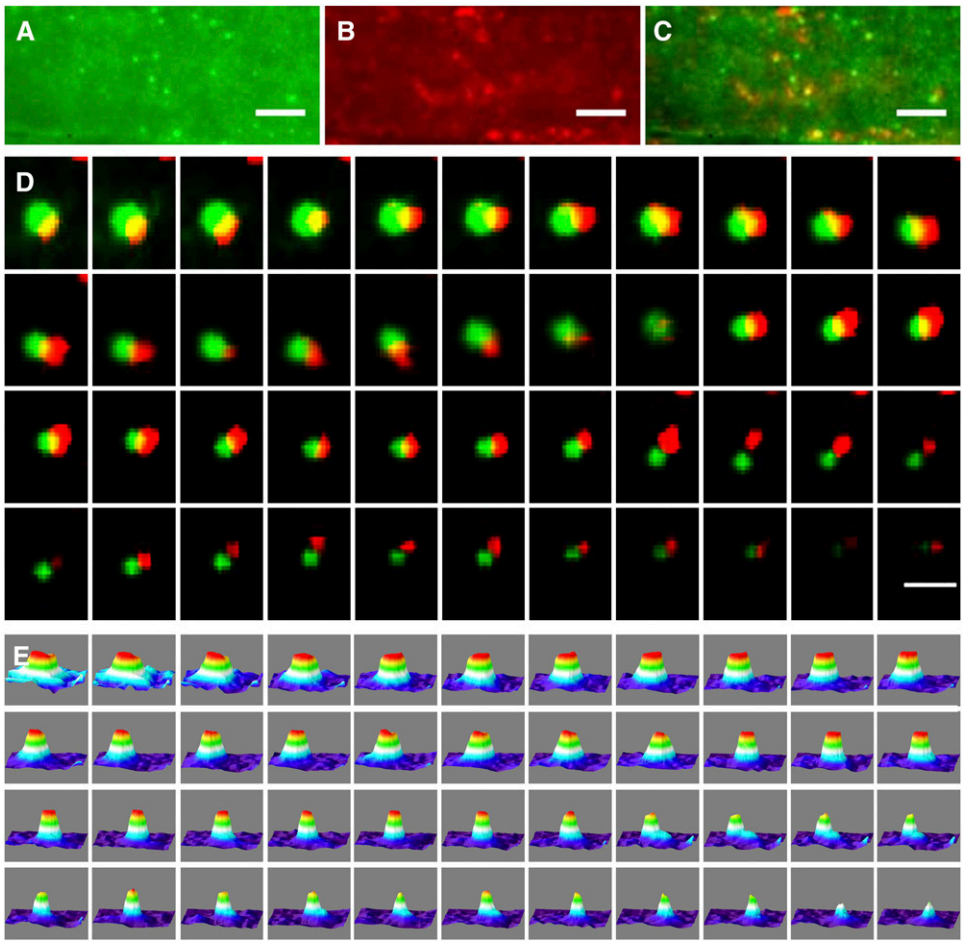

Figure 7. Colocalization and Codiffusion Analysis of PIP2;1 and CLC.

(A) EWM image of GFP-PIP2;1 clusters proximal to the plasma membrane.
(B) EWM image of mCherry-CLC clusters proximal to the plasma membrane.
(C) Merged image of **(A)** and **(B)**; the yellow dots indicate the colocalization particles.
(D) Time lapse showing an example of one overlapped GFP-PIP2;1 and mCherry-CLC spot codiffusion away from the focus.
(E) Three-dimensional luminance plots of the corresponding spots in **(D)**.
Bars = 5 μm in **(A)** to **(C)** and 1 μm in **(D)**.

stronger than that between GFP-PIP2;1 and mCherry-Flot1, consistent with the results obtained by EWM. When the seedlings were exposed to 100 mM NaCl, the interactions between GFP-PIP2;1/mCherry-CLC and GFP-PIP2;1/mCherry-Flot1 significantly increased. The relative cross-correlation amplitude was 0.59 ± 0.14 ($P < 0.01$) and 0.52 ± 0.08 ($P < 0.05$), revealing that the correlation between GFP-PIP2;1 and endocytic pathways became much stronger under hypertonic stress. Note that the increase in cross-correlation amplitude of GFP-PIP2;1/mCherry-Flot1 (23.8%) was higher compared with that of GFP-PIP2;1/mCherry-CLC (11.3%).

We then investigated the effects on GFP-PIP2;1 movement of tyrphostin A23 (TyrA23), a well-characterized inhibitor of the clathrin-mediated endocytic pathway (Dhonukshe et al., 2007). TyrA23 is thought to block specifically the interaction of endocytic cargo motifs with the clathrin medium chain. This interaction is crucial for establishing a link between the cytosolic domains of membrane proteins to the clathrin coat involved in vesicle formation (Banbury et al., 2003). Exposure of seedlings to TyrA23 led to an overall decrease in GFP-PIP2;1 diffusion coefficients, with $\hat{G}$ reduced to 1.59×10^{-3} $\mu m^2/s$ (SE 1.41 to 1.78×10^{-3} $\mu m^2/s$) (Figure 9A; see Supplemental Movie 6 online). The percentage of mixed trajectory after treatment with TyrA23 increased notably to twofold that of untreated control cells at the expense of Brownian and restricted diffusion, which decreased to 46 and 71%, respectively, of those in untreated control cells (Figure 9C). No obvious change in directed diffusion was detected (102% that of untreated control cells). Also, the effects of TyrA23 were found to be reversible; at 20 min after washout, the $\hat{G}$ value had increased to 2.20×10^{-3} $\mu m^2/s$ (SE 1.88 to 2.58×10^{-3} $\mu m^2/s$) (see Supplemental Figure 8A online), comparable to that of the control cells. When tyrphostin A51, an

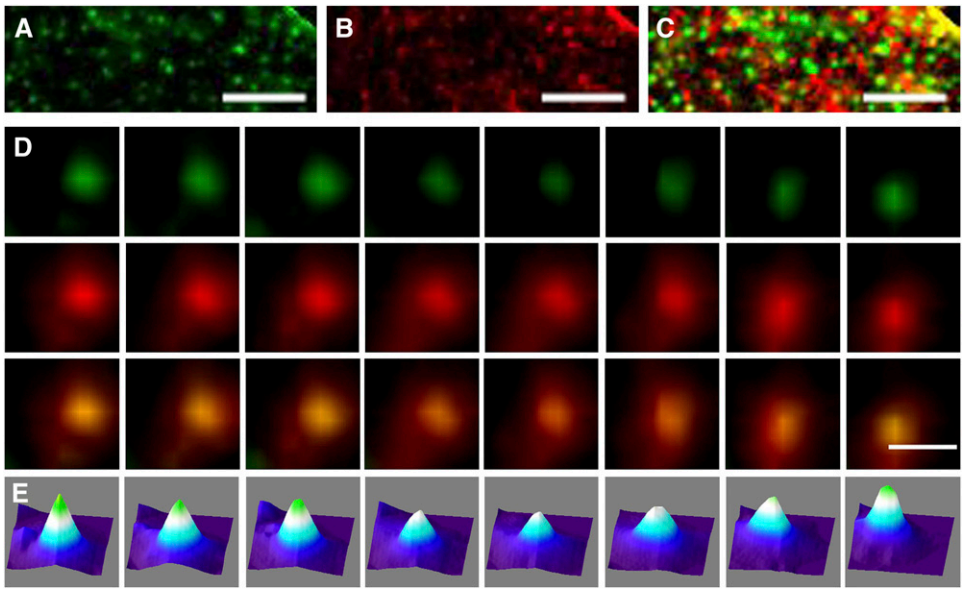

Figure 8. Colocalization and Codiffusion Analysis of PIP2;1 and Flot1.

(A) EWM image of GFP-PIP2;1 clusters proximal to the plasma membrane.
(B) EWM image of mCherry-Flot1 clusters proximal to the plasma membrane.
(C) Merged image of **(A)** and **(B)**; the yellow dots indicate the colocalization particles.
(D) An example of real-time dynamic observation of the GFP-PIP2;1 and mCherry-Flot1 molecule codiffusion.
(E) Three-dimensional luminance plots from the merged fluorescence of the corresponding spots in **(D)**.
Bars = 5 μm in **(A)** to **(C)** and 1 μm in **(D)**.

analog of TyrA23 that does not interfere with the clathrin–cargo interaction, was used (Banbury et al., 2003; Konopka et al., 2008), the diffusion coefficient of GFP-PIP2;1 did not change (see Supplemental Figure 8B online). The recovery experiment and noneffective analog treatment clearly suggested that the concentrations of TyrA23 used in this study were within the physiological range and its effect is rather specific.

Unlike in the presence of TyrA23, the histogram of diffusion coefficients after MβCD treatment showed a broad, bimodal distribution (Figure 9B; see Supplemental Movie 7 online), suggesting the existence of two subpopulations of diffusing GFP-PIP2;1 molecules. One subpopulation would correspond to molecules with a modal diffusion coefficient ($\hat{G} = 2.51 \times 10^{-3}$ $\mu m^2/s$, SE 2.32 to 2.73 $\times$ 10^{-3} $\mu m^2/s$) comparable to that observed under normal conditions. By contrast, most other GFP-PIP2;1 molecules diffused slowly with $\hat{G} = 1.26 \times 10^{-4}$ $\mu m^2/s$ (SE 1.01 to 1.57 $\times$ 10^{-4} $\mu m^2/s$), which was ~20 times lower. Among the GFP-PIP2;1 molecules analyzed after MβCD treatment, the percentage of Brownian diffusion declined to 67% of the untreated control cell value, and no obvious changes in the directed diffusion and mixed trajectory were detected (91 and 112% that of untreated control cells, respectively). In contrast with treatment with TyrA23, MβCD treatment increased the restricted diffusion to 164% that of untreated control cells (Figure 9C). These results demonstrate that treatment with TyrA23 and MβCD induced qualitatively different changes in GFP-PIP2;1 dynamic characteristics, suggesting that clathrin-dependent endocytosis and membrane rafts exerted different effects on PIP2;1 membrane movements under normal conditions.

The effects of TyrA23 and MβCD were also investigated in cells exposed to the salt treatment. When the roots were pretreated with TyrA23, the $\hat{G}$ of GFP-PIP2;1 decreased to 2.95×10^{-3} $\mu m^2/s$ (SE 2.62 to 3.33 $\times$ 10^{-3} $\mu m^2/s$) (Figure 9D; see Supplemental Movie 8 online) ($\hat{G} = 5.62 \times 10^{-3}$ $\mu m^2/s$ in the presence of salt alone). Brownian diffusion and restricted diffusion decreased to 78 and 67%, respectively, of the control treatment with salt alone; by contrast, the mixed trajectory increased to 183% of the control treatment with salt alone. No obvious change in directed diffusion was observed (Figure 9F). The tendencies for dynamic changes after treatment with TyrA23 under NaCl exposure were comparable to those after treatment with TyrA23 under normal conditions (cf. Figures 9C and 9F). When the roots were pretreated with MβCD, the bimodal repartition of the diffusion coefficient disappeared and $\hat{G}$ decreased to 2.63×10^{-3} $\mu m^2/s$ (SE 2.34 to 2.96 $\times$ 10^{-3} $\mu m^2/s$) (Figure 9E; see Supplemental Movie 9 online). In addition, Brownian diffusion and restricted diffusion decreased to 88 and 78% of the control treatment with salt alone, respectively. While the mixed trajectory increased to 150% of the control treatment with salt alone (Figure 9F), the percentage of directed diffusion was equal to the control treatment with salt alone. The tendencies in dynamic changes after treatment with MβCD under NaCl exposure were different from those after treatment with MβCD under normal conditions. However, they were similar to those after TyrA23 treatment under NaCl exposure, implying that inhibition of clathrin-dependent and membrane raft–associated endocytosis induced similar changes in PIP2;1 movement.

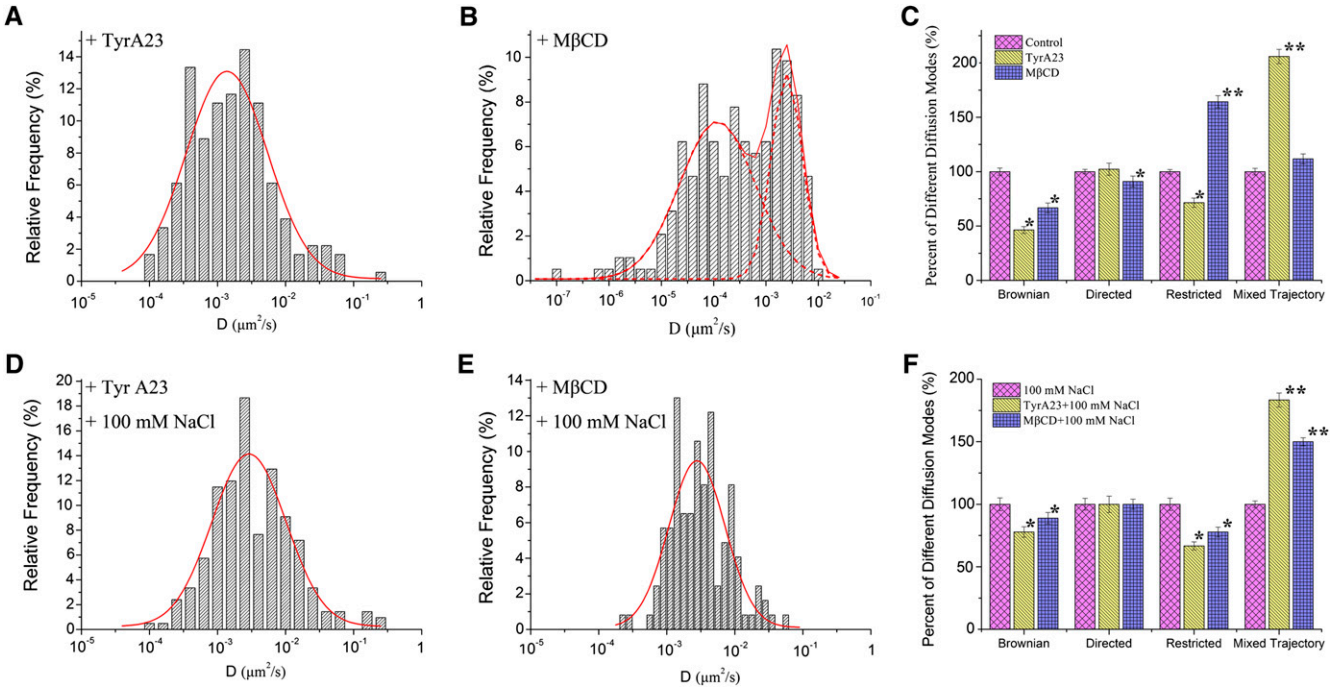

Figure 9. Histograms Showing the Dynamic Characteristics of GFP-PIP2;1 Molecules.

(A) Distribution of diffusion coefficients after treatment with TyrA23 (*n* = 180 spots).
(B) Distribution of diffusion coefficients after treatment with MβCD (*n* = 193 spots); the two peaks (dashed lines, Gaussian fit) indicate that the distribution of diffusion coefficients bifurcated.
(C) Percentage of different diffusion modes under TyrA23 (*n* = 96 individual trajectories) or MβCD treatment (*n* = 80 individual trajectories) compared with the percentage of control cells bathed in half-strength MS medium. Values given are mean ± SD.
(D) Distribution of diffusion coefficients after treatment with TyrA23 prior to exposure to 100 mM NaCl (*n* = 210 spots).
(E) Histogram showing the distribution of diffusion coefficients after treatment with MβCD coupled with 100 mM NaCl stimulus (*n* = 162 spots).
(F) Percentage of different diffusion modes of GFP-PIP2;1 in cells treated with TyrA23/MβCD prior to 100 mM NaCl exposure (*n* = 80 individual trajectories, respectively) compared with control cells bathed in 100 mM NaCl alone. **Significantly different from the control at $P < 0.01$; *significantly different from the control at $P < 0.05$, *t* test.
[See online article for color version of this figure.]

Disturbing the Endocytic Pathway Induces Accumulation of PIP2;1 on Plasma Membranes

To reveal the partitioning of PIP2;1 between the plasma membrane and its recycling pathways, FCS was used to measure the density of GFP-PIP2;1 in the plasma membrane under different conditions. FCS measurement was established by focusing an excitation laser beam onto the membrane and then monitoring fluorescence fluctuations within the focal volume of the laser beam (Figure 10A). Applying the parameters of Equation 4 gave an average density for GFP-PIP2;1 of 30.3 ± 5.1 molecules μm^{-2} (Figure 10B), indicating that an average of 11.5 GFP-PIP2;1 molecules occupied the 0.38-μm^2 area covered in the confocal volume. A higher GFP-PIP2;1 density (40.1 ± 7.2 molecules μm^{-2}; 32% increase with respect to control cells; $P < 0.05$, *t* test) was detected after treatment with TyrA23 (Figure 10B), indicating that more GFP-PIP2;1 molecules dwell on the membrane after the inhibition of clathrin-dependent endocytosis. By contrast, the density of PIP2;1 did not significantly change after treatment with MβCD (32.2 ± 5.4 molecules μm^{-2}; $P > 0.05$), Fen (30.2 ± 7.1 molecules μm^{-2}; $P > 0.05$), or PPMP (33.8 ± 8.2 molecules μm^{-2}; $P > 0.1$) (Figure 10B), suggesting that under normal conditions, disturbance of membrane rafts did not alter the amount of GFP-PIP2;1 molecules on the membrane. When the roots were exposed to 100 mM NaCl, the GFP-PIP2;1 density dropped to 14.0 ± 3.2 molecules μm^{-2} ($P < 0.001$; Figure 10B), implying that salt exposure induced internalization of PIP2;1. We also measured GFP-PIP2;1 molecular density after disturbing the endocytic pathways prior to exposure to 100 mM NaCl. Under TyrA23 pretreatment, and with respect to 100 mM NaCl alone, the density of GFP-PIP2;1 on plasma membranes significantly increased by ~50% to 21.1 ± 4.4 molecules μm^{-2} ($P < 0.01$; Figure 10B). After disrupting the membrane raft–associated endocytic pathway by a MβCD pretreatment, the density also significantly increased to 18.4 ± 3.0 molecules μm^{-2} ($P < 0.01$; Figure 10B), >30% higher than that of cells with salt alone. Pretreatments with Fen and PPMP also increased the density of GFP-PIP2;1 to 18.7 ± 7.0 molecules μm^{-2} ($P < 0.01$; Figure 10B) and 25.2 ± 6.2 molecules μm^{-2} ($P < 0.0001$; Figure 10B). These data indicate that both the clathrin-dependent and raft-associated endocytic pathways influenced endocytosis under 100 mM NaCl exposure conditions.

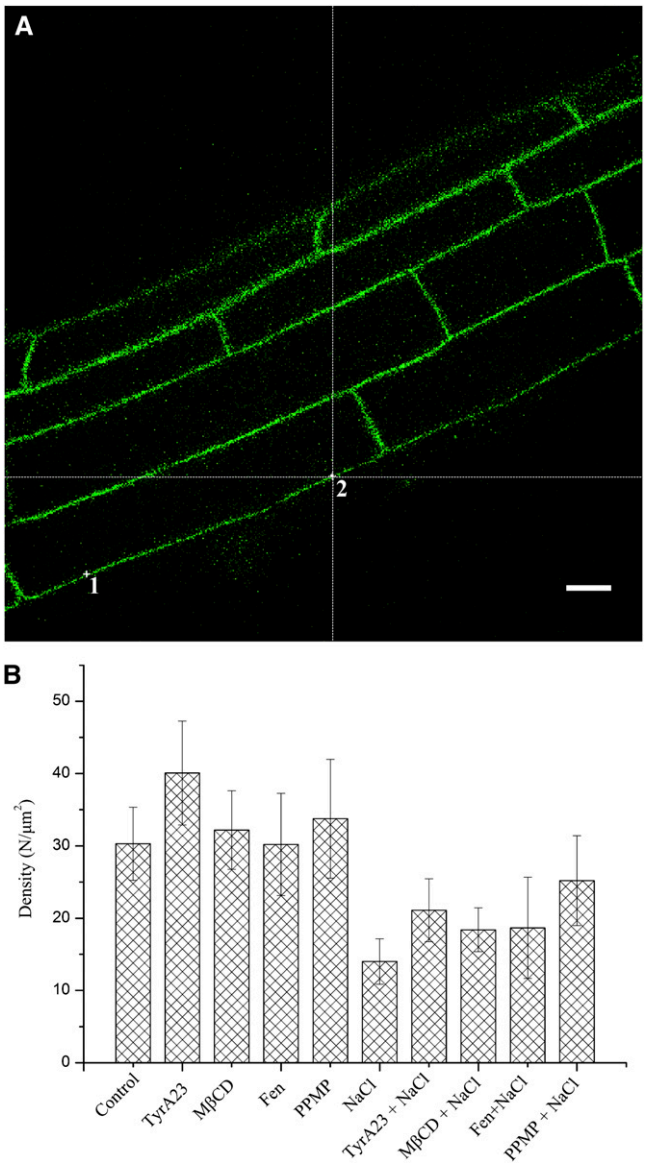

Figure 10. The Density of GFP-PIP2;1 Molecules under Different Conditions as Acquired with FCS.

(A) A confocal image detected by FCS; points 1 and 2 show the location where the laser beam was focused to monitor the fluorescence fluctuations. Bar = 10 μm.

(B) Density of GFP-PIP2;1 on the plasma membrane of epidermal cells under different conditions. Values given are mean ± SD.

[See online article for color version of this figure.]

DISCUSSION

Considering the complex and dynamic architecture of cell plasma membranes, the spatial and temporal dynamics of membrane proteins are definitely closely linked to many fundamental cellular processes (Shinozaki et al., 2009; Zhang et al., 2009b). In this respect, tracking protein dynamics using a single-molecule approach can be advantageous in deciphering the respective influence of protein interaction or microdomains on the lateral mobility of biomolecules, rather than submerging them into an assembly of characteristics. In this study, we used a high numerical aperture objective and varied the incident angle of the laser beam to obtain an exponentially decaying wave, exciting only fluorophores within 70 to 400 nm proximal to a glass cover slip. In terms of the signal-to-noise ratio, an evanescent wave microscope is up to 10-fold better than a confocal microscope (Wang et al., 2006). Equipped with a high-resolution EMCCD camera, which has extremely high temporal resolution, EWM could obtain near real-time images. Thus, EWM or variable-angle epifluorescence microscopy is an ideal tool for tracking the two-dimensional motion of cell membrane proteins in intact multicellular organisms (Konopka and Bednarek, 2008). This approach has provided valuable and complementary information about spot trafficking, especially in living cells, over lengthy observation periods (Konopka and Bednarek, 2008; Hern et al., 2010). In this investigation, we examined the dynamics and motion of GFP-labeled PIP2;1 molecules in living root cells of *Arabidopsis*. Thus, we achieved visualization of channel proteins at a single-molecule level in living plant cell membranes using EWM.

Since the discovery of aquaporins in plants, the study of these proteins has provided a unique perspective into multiple aspects of plant biology. Integrative (Ehlert et al., 2009) and cellular aspects (Van Wilder et al., 2008; Maurel et al., 2009; Gattolin et al., 2009) of plant–water relations and nutrition have been extensively investigated. However, the characteristics of plant aquaporins at the single-molecular level have remained unclear. Although the structure of aquaporins has been clarified using x-ray crystallography and cryoelectron microscopy (Jap and Li, 1995; Fotiadis et al., 2001; Törnroth-Horsefield et al., 2006), no studies had reported on the oligomeric state of PIPs in the plasma membrane of living plant cells. Here, we imaged GFP-labeled PIP2;1 in the plasma membrane of root cells to determine its oligomeric state. Since the fluorescence signals after expression using a native promoter were too weak to be detected for single-molecule analysis, overexpression of a fluorescently tagged construct was mandatory for this work. The genetic attachment of GFP to PIP2;1 obviated nonspecific labeling that might occur with antibodies and guaranteed that each PIP2;1 polypeptide was labeled with one, and only one, fluorophore. To interpret the oligomeric state of PIP2;1, we counted the photobleaching steps for each of the chosen fluorescent spots. In other channels or receptors (Ulbrich and Isacoff, 2007; Ji et al., 2008; Zhang et al., 2009c), the subunit number and stoichiometry of membrane-bound proteins can be determined from the statistical analysis of bleaching steps of GFP fused to the proteins. As shown in Figure 2, the number of elemental GFP photobleaching steps in an individual punctum was not uniform and ranged from one to four. Since the maximum number was four, a reasonable and conservative conclusion is that PIP2;1 exists on the membrane as a tetramer, in agreement with previous crystallographic studies (Törnroth-Horsefield et al., 2006). Moreover, as the fluorescence intensity distribution was skewed to intensities lower than four fluorophores, it may stem from endogenous unlabeled PIPs or some GFP-PIP2;1 with immature GFP being part of the oligomer. However, another possibility that cannot be excluded is that besides as a tetramer on the plasma membrane,

PIP2;1 exists in various multimeric forms, such as monomers, dimers, or trimers.

The lateral mobility of a molecule is of particular importance as it can be correlated with the molecular state as well as with environmental conditions (Pinaud et al., 2009). Although lateral diffusive mobility on the membrane of living cells has been measured by several means, such as fluorescent recovery after photobleaching, these methods provide only ensemble averaged information regarding the subpopulations, and determining the transition kinetics of diffusion mobility is impossible (Matsuoka et al., 2009). By applying EWM and SPT analysis, we found that the diffusion regime of PIP2;1 in plant cells could be classified into four categories: pure Brownian diffusion, restricted diffusion, directed diffusion, and mixed trajectory. The large dispersion of the diffusion coefficient distribution further confirmed that the diffusion of PIP2;1 on the membrane of root cells was highly heterogeneous. We also found that most of the fluorescent spots with low fluorescence intensity did not have a high diffusion coefficient, and there was no close correlation between the diffusion modes and the fluorescence intensity. However, this does not exclude the possibility that the oligomeric state exerts some effects on the protein motility. Considering that the separation of the membrane in distinct phases has significant effects on the lateral diffusion of a molecule (Korlach et al., 1999; Marguet et al., 2006), we can deduce that PIP2;1 is not uniformly localized in different plasma membrane microdomains. More importantly, PIP2;1 could move into or out of these microdomains, suggesting that the partitioning of PIP2;1 was dynamic. By tracking the motion of GFP-LTi6a, a small integral plasma membrane protein, we found that the diffusion coefficients of GFP-PIP2;1 and GFP-LTi6a were well within the range of various membrane intrinsic proteins reported previously (Cho et al., 1999), confirming that EWM and SPT analyses initially developed in mammalian cells (Loerke et al., 2009) can be similarly applied to plant cells. Comparison of diffusion coefficients of both proteins also revealed that GFP-LTi6a displayed strikingly faster lateral diffusion than GFP-PIP2;1. Whereas the diffusion mode of both proteins shares some common features, PIP2;1 exhibits some unique factors, which require further examination.

Current models of the plasma membrane predict the existence of a patchwork of specialized and dynamic microdomains coordinating a variety of cellular functions (Raffaele et al., 2009). Among the well-characterized plasma membrane microdomains are the membrane rafts formed by the preferential association of certain lipids and proteins into sterol- and glycosphingolipid-rich liquid ordered phases (also called detergent-resistant membranes) (Pinaud et al., 2009). Previous proteomic studies revealed a tendency of PIPs to partition in detergent-resistant membranes (membrane rafts) (Mongrand et al., 2004; Borner et al., 2005); however, whether this corresponds to an enrichment in true plasma membrane microdomains in living plant cells remained to be determined. To acquire a more detailed understanding of PIP2;1 partitioning in native membranes, we used the sterol-depleting drug, MβCD, and more specific inhibitors, Fen and PPMP, which affect the biosynthesis of sterol and sphingolipids. After treatment with these compounds, we observed a remarkable clustering effect of fluorescent foci and the disappearance of PIP2;1 molecules in certain areas, indicating that the partitioning of GFP-PIP2;1 is closely related to sterols and sphingolipids. Considering that sterols and sphingolipids promote the formation of membrane rafts and affect lipid dynamics on membranes, we speculated that the partitioning of PIP2;1 in the plasma membrane was associated with membrane rafts. To determine further if PIP2;1 was involved in membrane rafts, we adopted a general method called dynamic single-molecule colocalization, which was used to quantify the associations of single-cell surface molecules labeled with distinct fluorescent proteins, namely, GFP-PIP2;1 and mCherry-Flot1 (taken here as a raft marker). The chief advantages of the new quantitative approach were that in addition to stable interactions, it was capable of measuring nonconstitutive associations and was applicable to situations with low numbers of molecules. In cells that coexpressed GFP-PIP2;1 and mCherry-Flot1, we observed that some PIP2;1 fluorescent foci were colocalizing with Flot1 foci and that the joint movement of these molecules was mainly confined to specific areas, suggesting that it was correlated with entry into or interaction with quasistationary membrane rafts. The results provide strong evidence that lipid microdomains are involved in confining PIP2;1 in the plasma membrane.

Recent studies have pointed to protein trafficking as a critical point in regulating plant aquaporin function. This process contributes to diverse responses, such as nutritional adjustments and modification of the number of active proteins at the plasma membrane (Takano et al., 2005). PIP molecules are subject to constitutive cycling between the plasma membrane and cytoplasm through processes of endo- and exocytosis (reviewed in Maurel et al., 2009). In addition, the alteration of PIP abundance at the plasma membrane through stimulus-induced trafficking of PIPs is a significant mechanism to regulate root water transport (Boursiac et al., 2005, 2008; Maurel et al., 2009). We observed a salt-induced intracellular accumulation of GFP-PIP2;1 and a reduced membrane density. Given that the intracellular accumulation of GFP-LTi6a was much less pronounced, we propose that the enhanced internalization was a specific response of GFP-PIP2;1 under hypertonic stress, acting as a regulator to protect cells or the plant against water-deficit stress. SPT analysis further revealed that under these conditions, the diffusion coefficient and the percentage of restricted diffusion dramatically increased. From these results, we conclude that PIP2;1 undergoing enhanced endocytosis is characterized by an increased diffusion coefficient and that spatially restricted diffusion is an important feature of the endocytic process. In agreement with this, restricted diffusion was reported to be a predominant diffusion mode in internalized QD–NGF complexes (Rajan et al., 2008).

In this work, we also dissected the endocytic pathway(s) of PIP2;1 by analyzing the effects of specific inhibitors. TyrA23 can specifically prevent the interaction between cargo motifs destined for endocytosis and the μ2 subunit of the clathrin binding AP-2 adaptor complex (Banbury et al., 2003). A recent report showed that TyrA23 efficiently inhibited interaction between the human transferrin receptor and a μ-adaptin subunit and then blocked the internalization of the human transferrin receptor in *Arabidopsis* protoplasts (Ortiz-Zapater et al., 2006). Thus, it is widely used to inhibit clathrin-dependent endocytosis without causing discernible morphological changes (Dhonukshe et al., 2007; Robinson et al., 2008). Previous investigations demonstrated that the

accumulation of PIP2;1 in the Brefeldin A compartment was inhibited by TyrA23, suggesting that clathrin might be involved in PIP2;1 endocytic mechanisms (Dhonukshe et al., 2007). The colocalization of GFP-PIP2;1 with mCherry-CLC and an increase in PIP2;1 density in the plasma membrane after TyrA23 treatment reported in this study further support this conclusion. SPT analysis of diffraction-limited fluorescent spots also showed that the repartitioning of diffusion modes and changes in diffusion coefficients induced by TyrA23 were counteracted in the presence of NaCl. Given the link between NaCl treatment and enhanced internalization of PIP2;1, we inferred that the changes after TyrA23 treatment resulted mainly from the inhibition of endocytosis and that the internalization of PIP2;1 under both normal and salt stress conditions was predominantly associated with the clathrin-dependent pathway.

Besides clathrin-dependent endocytosis, other entry pathways are considered to operate in plant cells, among which membrane raft-associated endocytosis is an important form (Murphy et al., 2005). The raft-associated pathway, defined as a sterol-sensitive and clathrin-independent internalization of cargoes from the plasma membrane, is considered to be a new route of endocytosis (Lajoie and Nabi, 2007). Sterol-dependent endocytosis has been reported to mediate postcytokinetic acquisition of PIN2 auxin efflux carrier polarity in *Arabidopsis* (Men et al., 2008). Since we found that the partitioning of PIP2;1 on the plasma membrane was closely associated with membrane rafts, we were also curious as to whether the uptake mechanism of PIP2;1 from the plasma membrane was related to these membrane domains. SPT analysis showed that in seedlings with MβCD under normal conditions, diffusion coefficients of PIP2;1 became bifurcated, suggesting that two different pools of PIP2;1 were segregated into different membrane domains. Considering that sterol depletion induces different changes in the continuous nonraft phase and stationary microdomains, respectively, the bifurcated diffusion coefficients confirmed the aforementioned conclusion that the partitioning of PIP2;1 was associated with a type of membrane rafts. FCS also indicated that under normal conditions, MβCD treatment did not change PIP2;1 density at the plasma membranes. Thus, in contrast with their important role in PIP2;1 partitioning, membrane rafts made a low contribution to internalization under normal conditions.

When seedlings were treated with MβCD together with 100 mM NaCl, SPT analysis showed that the repartitioning of different diffusion modes and changes in diffusion coefficients were similar to those observed after a TyrA23 plus NaCl treatment. TyrA23 was somewhat able to counteract the effects of NaCl exposure; similarly, MβCD pretreatment significantly increased the plasma membrane density of PIP2;1 in NaCl-treated cells. Thus, we can reasonably conclude that under salt stress, the membrane raft–associated pathway was stimulated and contributed to the enhanced internalization of PIP2;1. The FCCS quantitative analysis presented in this work also suggested that the contribution of raft-associated components to PIP2;1 cell dynamics is greater under salt stress than under control conditions. In fact, the combined effects of two endocytic pathways have already been observed in animals (Schneider et al., 2008). Our data suggest along these lines that the stimulated endocytosis of PIP2;1 under salt stress depends on the action of clathrin-dependent and membrane raft–associated pathways simultaneously.

In conclusion, this work shows that EWM detection and SPT analysis can substantially enhance our understanding of plant plasma membrane protein dynamics. The study also revealed previously undiscovered associations between membrane dynamics and the regulation properties of PIP2;1, a major plant aquaporin. The behavior of PIP2;1 in the plasma membrane of living cells was highly heterogeneous and could be described using four diffusion categories; moreover, membrane rafts were found to play an important role in the membrane partitioning of PIP2;1. Whereas clathrin-dependent endocytosis of PIP2;1 was predominant under normal conditions, a membrane raft–associated pathway was also involved under NaCl stress. Thus, stress-induced changes in PIP2;1 density at the plant plasma membrane do not rely on a unimodal endocytosis as the mechanism of uptake, as summarized in Figure 11. Taken together, these findings provide new insights into the regulation mechanisms of PIP2;1 through dynamic partitioning on the membrane and alternate recycling pathways.

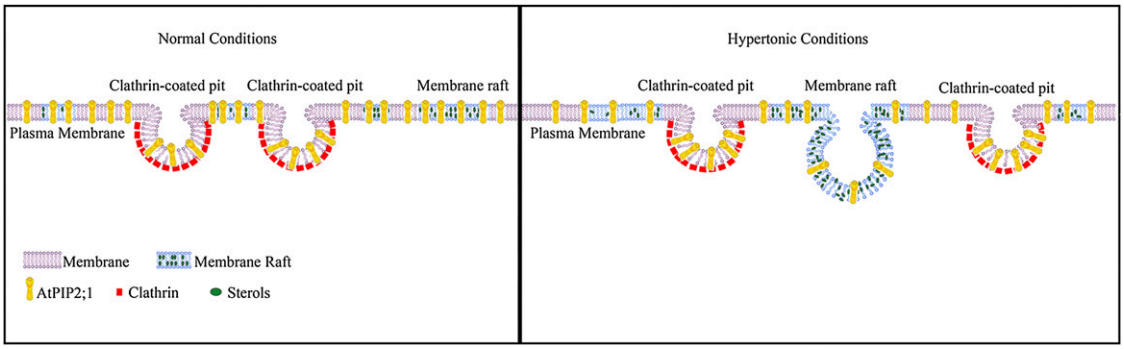

Figure 11. Hypothetical Model Summarizing the Endocytic Pathway of PIP2;1 under Normal and Hypertonic Conditions.

Under normal conditions, the constitutive cycling of PIP2;1 is mediated mainly by clathrin-coated pits. Under hypertonic conditions, however, the enhanced cycling of PIP2;1 depends on simultaneous internalization through clathrin-dependent and membrane raft–associated pathways.

METHODS

Plant Culture and Transformation

A *GFP-PIP2;1* plant expression vector was constructed as follows. The coding sequence for At-PIP2;1 was PCR amplified using the primers 5′-TCTAGAATGGCAAAGGATGTGGAAGCCGTTC-3′ and 5′-GTCGAC-TTAGACGTTGGCAGCACTTCTGAAT-3′ and was subcloned as a *Xba*I-*Sal*I fragment into a modified pCAMBIA2300 vector (Hajdukiewicz et al., 1994). The *mCherry-AtFlot1* and *mCherry-CLC* (At2g40060) plant expression vectors were constructed with the coding sequences for Flot1 and CLC, which were PCR amplified using specific primer pairs (*Flot1*, 5′-GGATCCATGTTCAAAGTTGCAAG-3′ and 5′-GAATTCTTAGCTGC-GAGTCACTT-3′; *CLC*, 5′-GGATCCATGTCTGCCTTTGAAGACGATT-CCT-3′ and 5′-GAATTCTTAAGCAGCAGTAACTGCCTCAGTG-3′) and subcloned as *Bam*HI-*Eco*RI fragments into a modified pCAMBIA1200 vector (Hajdukiewicz et al., 1994).

Arabidopsis thaliana ecotype Columbia wild type was transformed with the *GFP-PIP2;1*, *mCherry-Flot1*, and *mCherry-CLC* constructs using the *Agrobacterium tumefaciens*–mediated floral dip method (Clough and Bent, 1998). The preparation of plants expressing a GFP-LTi6a is described elsewhere (Cutler et al., 2000). Transgenic plants were selected on solid medium (1% agar), half-strength Murashige and Skoog (MS) salts medium containing 50 μg/mL kanamycin for GFP-PIP2;1, and 70 μg/mL hygromycin for mCherry-Flot1 and mCherry-CLC.

Seeds were surface sterilized for 2 min in 70% ethanol, transferred to 5% (w/v) NaClO for 15 min, and then washed five times with sterilized distilled water. Subsequently, they were transferred to a thin layer of solid medium containing half-strength MS salts with 0.7% plant agar. Plants were cultured at 22°C under long-day conditions (16 h light, 8 h dark) for 4 d.

Drug Treatment

The stock solution of MβCD (Sigma-Aldrich) was prepared in deionized water. TyrA23 (Sigma-Aldrich) was dissolved in 100% DMSO to yield a 50 mM stock solution. The inhibitors were diluted in half-strength MS medium, and the final DMSO concentration was ≤0.1% (v/v) in all EWM analyses. Vertically grown 4-d-old seedlings were incubated in half-strength liquid MS medium containing 50 μM TyrA23 or 10 mM MβCD for 30 min. For the TyrA23 washout experiment, the seedlings were first incubated in half-strength liquid MS medium containing 50 μM TyrA23 for 30 min, transferred to media without TyrA23 for 20 min, then observed under EWM. For the treatment with Fen, seedlings were grown vertically on half-strength MS, 0.7% agar plates with 10 μg/mL Fen for 4 d prior to imaging in half-strength MS media. For treatment with PPMP, the seedlings first grew on half-strength MS agar medium for 2 d and then the 2-d-old seedlings were transferred to MS agar medium with 10 μM PPMP to grow for another 2 d.

The effects of NaCl were studied by supplementing the half-strength MS medium with 100 mM NaCl. Parallel experiments with sorbitol were performed by supplementing the half-strength MS medium with 200 mM sorbitol. The effects of TyrA23 and MβCD under 100 mM NaCl exposure were studied by pretreatment with 50 μM TyrA23 or 10 mM MβCD for 30 min followed by incubation in the same solution but supplemented with 100 mM NaCl. After the indicated times, seedlings were transferred to a glass slide with 150 μL of inhibitor solution and covered with a cover slip.

Confocal Laser Scanning Microscopy Observations

For FM4-64 staining, 4-d-old vertically grown seedlings were transferred to 2.5 μM FM4-64 diluted in half-strength MS medium for 3 min after being exposed to 100 mM NaCl for 10 min. Then these seedlings were observed under confocal laser scanning microscopy.

Single-Molecule Fluorescence Imaging

An objective-type evanescent wave microscope, which was based on an inverted microscope (IX-71; Olympus) with a total internal reflective fluorescence illuminator and a ×100 oil-immersion objective (Olympus; numerical aperture = 1.45), was used for single-molecule fluorescence imaging. The 473-nm/561-nm laser line from a diode laser (Changchun New Industries Optoelectronics Technology) was used to excite GFP and mCherry. Fluorescence signals were collected by the objective and passed through two filters, a BA 510IF long-pass filter (Chroma) and an HQ525/50 band-pass filter (Chroma), before being directed using a back-illuminated, EMCCD camera (ANDOR iXon DV8897D-CS0-VP; Andor Technology) and high-quality filters (band-pass 525/45 and 609/54 nm). We set the gain of our EMCCD camera at 300 throughout all single-molecule imaging experiments; the setting was in the linear dynamic range of the EMCCD camera. Images were acquired with 100-ms exposure time and analyzed with Image J software (NIH).

Image Analysis and Tracking of Single Molecules

Time-lapse series of single particles of GFP-PIP2;1 images were taken at up to 200 images per sequence. For the analysis of single-molecule fluorescence intensity in a movie acquired from living cells, the background fluorescence was first subtracted from each frame using the rolling ball method in Image J software. Then, the first frame of each movie was used for fluorescent spot (region of interest) selection. After the image processing, the brightest pixel in each fluorescent spot within the diffraction-limited size (3 × 3 pixels) was determined as the central position, and a square of 3 × 3 pixels was enclosed as a region of interest to calculate the integrated fluorescence intensity with Image J.

To analyze dynamic properties, GFP-PIP2;1 foci were tracked using spatially and temporally global particle assignment, described in detail elsewhere (Jaqaman et al., 2008). We analyzed the MSD of fluorescence-labeled PIP2;1 spots using the following equation:

$$\mathrm{MSD} = (x - x_0)^2 + (y - y_0)^2 \quad (1)$$

where x_0 and y_0 are the initial coordinates, and x and y are the coordinates at any given time (Haggie and Verkman, 2008).

For calculating the diffusion coefficient, we plotted MSD from each trajectory against time. For each molecule, the slope of the first four time points in the MSD-*t* plot was used to calculate the diffusion coefficient (*D*) according to the following equation (Xiao et al., 2008):

$$\mathrm{MSD}_{t\to 0} = 4Dt \quad (2)$$

In the text, the diffusion coefficients correspond to single (or multiple) Gaussian fit(s) of the D-histograms. The SE values of the position of the peak (noted as $\hat{G}$) were determined using Origin software (OriginLab) and are given in the form of an upper and lower diffusion coefficient. Determination of the motional modes (Brownian, restricted, directed diffusion, or mixed trajectory) and parameters was performed according to Espenel et al. (2008). For each trajectory, we first linearly fit the MSD. If the MSD-*t* plot was a straight line with a slope of 4D, it was a typical trajectory for spots undergoing Brownian diffusion. If the MSD-*t* plot showed a positive or negative deviation from a straight line with a slope of 4D, the motion was determined as directed or restricted diffusion. For the mixed trajectory exhibiting a combination of Brownian and apparent restricted diffusion mode, the trajectory was split, and the MSD of each segment was adjusted with a linear or an exponential curve. In a few cases, no convincing MSD-*t* fits could be obtained, and the trajectories were rejected.

The range of an individual fluorescent spot movement during the time interval (Tn) can be estimated from the following equation:

$$\mathrm{Range}(n) = \sqrt{[x_n - x_{(n-1)}]^2 + [y_n - y_{(n-1)}]^2} \quad (3)$$

The colocalization algorithm was obtained using the Image J plugins Colocalization Test and Colocalization Threshold of T. Collins and

W. Rasband, and BG Subtraction from ROI from M. Cammer and T. Collins (www.uhnresearch.ca/facilities/wcif/imagej). Colocalization was performed as previously described (Zhang et al., 2009a).

FCS Analyses

FCS was performed on a Leica TCS SP5 FCS microscope, equipped with a 488-nm argon laser, in-house coupled correlator, and Avalanche photodiode. After acquiring a scan image of cells in transmitted light mode, FCS was performed in the point-scanning mode. The laser focus was placed at the plasma membrane of a cell. The diffusion of fluorophores into and out of the focal volume alters the local concentration of fluorophores and thus leads to spontaneous fluorescence intensity fluctuations.

The autocorrelation function G(τ) was calculated with the hardware correlator as $[\delta F(t)\ \delta F(t+\tau)]/[F(t)]^2$, where $F(t)$ is the fluorescence fluctuation caused by a particle entering the confocal volume and $F(t+\tau)$ is the fluorescence fluctuation by the same particle at time $(t+\tau)$. IgorPro software was used to fit the data to the two-dimensional one particle, one-triplet (2D1P1t) models as follows:

$$G(\tau) = \frac{1}{N} \times \left[\left\{ \frac{1}{(1+\tau/\tau D)} \right\} \left\{ 1 + \frac{F_{trip}}{(1-F_{trip})} \times e^{-(\tau/\tau_{trip})} \right\} \right] + 1 \qquad (4)$$

where N is the number of particles in the observation volume, F_{trip} is the fraction of particles in the triplet state, and t_{trip} is the triplet relaxation time.

When the volume element was projected onto a single cell, GFP-labeled PIP2;1 localized in the cell membrane was observed. Thus, the parameter N, which could be obtained by fitting the autocorrelation function, characterized the total number of GFP-PIP2;1 proteins in the cell membrane inside the confocal volume. The dimensions of the observation volume element were defined by the half-axes for length (ω_z) and width (ω_{xy}). The waist of the confocal volume ellipsoid was assumed to be situated on the cell membrane such that the highest fluorescence intensity was given. In this case, the surface area on the membrane covered by the focus would be a circular area with a radius equal to ω_{xy}. The circular area covered by the focus volume could be estimated as $\pi(\omega_{xy})^2 = \pi \times (0.35\ \mu m)^2 = 0.38\ \mu m^2$. Therefore, the GFP-PIP2;1 density estimated in the confocal volume could be expressed as the total number of GFP-PIP2;1 divided by the area covered as follows:

$$\text{Density} = N \Big/ \left[\pi (\omega_{xy})^2 \right] \qquad (5)$$

The GFP-PIP2;1 density was obtained from each individual cell membrane. Two random positions were selected once, and an autocorrelation measurement was performed for 20 s each for every single measurement point. Up to six random points were selected in one cell, three cells were chosen in a root, and at least five representative roots were studied for each measurement.

For quantitatively evaluating the interaction of GFP-PIP2;1/mCherry-Flot1 and GFP-PIP2;1/mCherry-CLC, FCCS was performed. The amplitude of the cross-correlation function was normalized to the amplitude of the autocorrelation function of GFP to calculate the relative cross-correlation ($[Gc(0)]/[Gg(0)]$), as described in a previous investigation (Noda et al., 2008). Up to six random points were selected in one cell, five cells were chosen in a root, and at least three representative roots were studied for each measurement.

Accession Numbers

Sequence data from this article can be found in The Arabidopsis Information Resource database under the following accession numbers: PIP2;1 (At3g53420), Flot1 (At5g25250), and CLC (At2g40060).

Supplemental Data

The following materials are available in the online version of this article.

Supplemental Figure 1. EWM Detection of the GFP Fluorescence Signal.

Supplemental Figure 2. The Dynamic Characteristics of GFP-Labeled PIP2;1 Spots Plotted against the Fluorescence Intensity.

Supplemental Figure 3. Automated Tracking and Statistical Analysis of GFP-LTi6a Spots on the Plasma Membrane.

Supplemental Figure 4. Sterol Content of Plasma Membranes Labeled with Filipin.

Supplemental Figure 5. Organization of the Actin Cytoskeleton in Control (Untreated) and MβCD-Treated Seedlings.

Supplemental Figure 6. Characteristics of the GFP-PIP2;1 Partitioning on the Plasma Membrane after Treatment with Fen and PPMP.

Supplemental Figure 7. Parallel Experiments Using Seedlings Expressing GFP-PIP2;1 or GFP-LTi6a as a Plasma Membrane Marker and Treated with Salt or Sorbitol as a Comparable Osmotic Stress.

Supplemental Figure 8. Distribution of Diffusion Coefficients for GFP-PIP2;1 on the Plasma Membrane of Epidermal Cells after TyrA23 Washout and TyrA51 Treatment.

Supplemental Table 1. Comparison of Actin Dynamic Parameters from Control and MβCD-Treated Root Cells.

Supplemental Movie 1. Dynamics of GFP-Labeled PIP2;1 on the Plasma Membrane Driven by the Native Promoter.

Supplemental Movie 2. Dynamics of GFP-PIP2;1 on the Plasma Membrane under Normal Conditions Detected by EWM.

Supplemental Movie 3. Dynamics of the Actin Cytoskeleton in Control (Untreated) Seedlings.

Supplemental Movie 4. Dynamics of the Actin Cytoskeleton in MβCD-Treated Seedlings.

Supplemental Movie 5. Dynamics of GFP-PIP2;1 on the Plasma Membrane under Salt Stress Detected by EWM.

Supplemental Movie 6. Dynamics of GFP-PIP2;1 on the Plasma Membrane after Treatment with TyrA23 Detected by EWM.

Supplemental Movie 7. Dynamics of GFP-PIP2;1 on the Plasma Membrane after Treatment with MβCD Detected by EWM.

Supplemental Movie 8. Dynamics of GFP-PIP2;1 on the Plasma Membrane after Treatment with TyrA23 Coupled with a 100 mM NaCl Stimulus.

Supplemental Movie 9. Dynamics of GFP-PIP2;1 on the Plasma Membrane after Treatment with MβCD Coupled with a 100 mM NaCl Stimulus.

ACKNOWLEDGMENTS

We thank Wei Ji and Wangxi Luo for technical assistance with EWM as well as Yinglang Wan and Lusheng Fan for their valuable comments on data analysis and early drafts of this manuscript. This work is supported by the National Basic Research Program of China (973 Program 2011CB809103 and 2007CB108703), the Chinese Academy of Sciences/State Administration of Foreign Experts Affairs International Partnership Program for Creative Research Teams (20090491019), the National Natural Science Foundation of China (30730009, 30821007, and 30900072), and the Knowledge Innovation Program of the Chinese Academy of Sciences (KJCX2-YW-L08 and KSCX2-EW-J-1).

AUTHOR CONTRIBUTIONS

X.L. and J.L. designed the research. X.L., R.L., D.-T.L., and C.M. performed the experiments. X.L., X.W., and Y.Y. analyzed data. Q.H.

and X.F. contributed new analytic tools. X.L, D.-T.L., C.M., and J.L. wrote the article.

Received September 9, 2011; revised September 9, 2011; accepted October 3, 2011; published October 18, 2011.

REFERENCES

Banbury, D.N., Oakley, J.D., Sessions, R.B., and Banting, G. (2003). Tyrphostin A23 inhibits internalization of the transferrin receptor by perturbing the interaction between tyrosine motifs and the medium chain subunit of the AP-2 adaptor complex. J. Biol. Chem. **278:** 12022–12028.

Bhat, R.A., and Panstruga, R. (2005). Lipid rafts in plants. Planta **223:** 5–19.

Biela, A., Grote, K., Otto, B., Hoth, S., Hedrich, R., and Kaldenhoff, R. (1999). The *Nicotiana tabacum* plasma membrane aquaporin NtAQP1 is mercury-insensitive and permeable for glycerol. Plant J. **18:** 565–570.

Borner, G.H., Sherrier, D.J., Weimar, T., Michaelson, L.V., Hawkins, N.D., Macaskill, A., Napier, J.A., Beale, M.H., Lilley, K.S., and Dupree, P. (2005). Analysis of detergent-resistant membranes in *Arabidopsis*. Evidence for plasma membrane lipid rafts. Plant Physiol. **137:** 104–116.

Boursiac, Y., Boudet, J., Postaire, O., Luu, D.T., Tournaire-Roux, C., and Maurel, C. (2008). Stimulus-induced downregulation of root water transport involves reactive oxygen species-activated cell signalling and plasma membrane intrinsic protein internalization. Plant J. **56:** 207–218.

Boursiac, Y., Chen, S., Luu, D.T., Sorieul, M., van den Dries, N., and Maurel, C. (2005). Early effects of salinity on water transport in *Arabidopsis* roots. Molecular and cellular features of aquaporin expression. Plant Physiol. **139:** 790–805.

Chaumont, F., Moshelion, M., and Daniels, M.J. (2005). Regulation of plant aquaporin activity. Biol. Cell **97:** 749–764.

Cho, M.R., Knowles, D.W., Smith, B.L., Moulds, J.J., Agre, P., Mohandas, N., and Golan, D.E. (1999). Membrane dynamics of the water transport protein aquaporin-1 in intact human red cells. Biophys. J. **76:** 1136–1144.

Clough, S.J., and Bent, A.F. (1998). Floral dip: A simplified method for *Agrobacterium*-mediated transformation of *Arabidopsis thaliana*. Plant J. **16:** 735–743.

Cutler, S.R., Ehrhardt, D.W., Griffitts, J.S., and Somerville, C.R. (2000). Random GFP:cDNA fusions enable visualization of subcellular structures in cells of *Arabidopsis* at a high frequency. Proc. Natl. Acad. Sci. USA **97:** 3718–3723.

Dahan, M., Lévi, S., Luccardini, C., Rostaing, P., Riveau, B., and Triller, A. (2003). Diffusion dynamics of glycine receptors revealed by single-quantum dot tracking. Science **302:** 442–445.

Dhonukshe, P., Aniento, F., Hwang, I., Robinson, D.G., Mravec, J., Stierhof, Y.D., and Friml, J. (2007). Clathrin-mediated constitutive endocytosis of PIN auxin efflux carriers in *Arabidopsis*. Curr. Biol. **17:** 520–527.

Douglass, A.D., and Vale, R.D. (2005). Single-molecule microscopy reveals plasma membrane microdomains created by protein-protein networks that exclude or trap signaling molecules in T cells. Cell **121:** 937–950.

Ehlert, C., Maurel, C., Tardieu, F., and Simonneau, T. (2009). Aquaporin-mediated reduction in maize root hydraulic conductivity impacts cell turgor and leaf elongation even without changing transpiration. Plant Physiol. **150:** 1093–1104.

Espenel, C., Margeat, E., Dosset, P., Arduise, C., Le Grimellec, C., Royer, C.A., Boucheix, C., Rubinstein, E., and Milhiet, P.E. (2008). Single-molecule analysis of CD9 dynamics and partitioning reveals multiple modes of interaction in the tetraspanin web. J. Cell Biol. **182:** 765–776.

Fetter, K., Van Wilder, V., Moshelion, M., and Chaumont, F. (2004). Interactions between plasma membrane aquaporins modulate their water channel activity. Plant Cell **16:** 215–228.

Foresti, O., Gershlick, D.C., Bottanelli, F., Hummel, E., Hawes, C., and Denecke, J. (2010). A recycling-defective vacuolar sorting receptor reveals an intermediate compartment situated between prevacuoles and vacuoles in tobacco. Plant Cell **22:** 3992–4008.

Fotiadis, D., Jenö, P., Mini, T., Wirtz, S., Müller, S.A., Fraysse, L., Kjellbom, P., and Engel, A. (2001). Structural characterization of two aquaporins isolated from native spinach leaf plasma membranes. J. Biol. Chem. **276:** 1707–1714.

Gattolin, S., Sorieul, M., Hunter, P.R., Khonsari, R.H., and Frigerio, L. (2009). *In vivo* imaging of the tonoplast intrinsic protein family in *Arabidopsis* roots. BMC Plant Biol. **9:** 133.

Haggie, P.M., and Verkman, A.S. (2008). Monomeric CFTR in plasma membranes in live cells revealed by single molecule fluorescence imaging. J. Biol. Chem. **283:** 23510–23513.

Hajdukiewicz, P., Svab, Z., and Maliga, P. (1994). The small, versatile pPZP family of *Agrobacterium* binary vectors for plant transformation. Plant Mol. Biol. **25:** 989–994.

Hern, J.A., Baig, A.H., Mashanov, G.I., Birdsall, B., Corrie, J.E., Lazareno, S., Molloy, J.E., and Birdsall, N.J. (2010). Formation and dissociation of M1 muscarinic receptor dimers seen by total internal reflection fluorescence imaging of single molecules. Proc. Natl. Acad. Sci. USA **107:** 2693–2698.

Jap, B.K., and Li, H. (1995). Structure of the osmo-regulated H_2O-channel, AQP-CHIP, in projection at 3.5 A resolution. J. Mol. Biol. **251:** 413–420.

Jaqaman, K., Loerke, D., Mettlen, M., Kuwata, H., Grinstein, S., Schmid, S.L., and Danuser, G. (2008). Robust single-particle tracking in live-cell time-lapse sequences. Nat. Methods **5:** 695–702.

Ji, W., Xu, P., Li, Z., Lu, J., Liu, L., Zhan, Y., Chen, Y., Hille, B., Xu, T., and Chen, L. (2008). Functional stoichiometry of the unitary calcium-release-activated calcium channel. Proc. Natl. Acad. Sci. USA **105:** 13668–13673.

Joo, C., Balci, H., Ishitsuka, Y., Buranachai, C., and Ha, T. (2008). Advances in single-molecule fluorescence methods for molecular biology. Annu. Rev. Biochem. **77:** 51–76.

Katsuhara, M., Hanba, Y.T., Shiratake, K., and Maeshima, M. (2008). Expanding roles of plant aquaporins in plasma membranes and cell organelles. Funct. Plant Biol. **35:** 1–14.

Konopka, C.A., Backues, S.K., and Bednarek, S.Y. (2008). Dynamics of *Arabidopsis* dynamin-related protein 1C and a clathrin light chain at the plasma membrane. Plant Cell **20:** 1363–1380.

Konopka, C.A., and Bednarek, S.Y. (2008). Variable-angle epifluorescence microscopy: A new way to look at protein dynamics in the plant cell cortex. Plant J. **53:** 186–196.

Korlach, J., Schwille, P., Webb, W.W., and Feigenson, G.W. (1999). Characterization of lipid bilayer phases by confocal microscopy and fluorescence correlation spectroscopy. Proc. Natl. Acad. Sci. USA **96:** 8461–8466.

Lajoie, P., and Nabi, I.R. (2007). Regulation of raft-dependent endocytosis. J. Cell. Mol. Med. **11:** 644–653.

Lee, H.K., Cho, S.K., Son, O., Xu, Z., Hwang, I., and Kim, W.T. (2009). Drought stress-induced Rma1H1, a RING membrane-anchor E3 ubiquitin ligase homolog, regulates aquaporin levels via ubiquitination in transgenic *Arabidopsis* plants. Plant Cell **21:** 622–641.

Loerke, D., Mettlen, M., Yarar, D., Jaqaman, K., Jaqaman, H.,

Danuser, G., and Schmid, S.L. (2009). Cargo and dynamin regulate clathrin-coated pit maturation. PLoS Biol. **7:** e57.

Marguet, D., Lenne, P.F., Rigneault, H., and He, H.T. (2006). Dynamics in the plasma membrane: how to combine fluidity and order. EMBO J. **25:** 3446–3457.

Martre, P., Morillon, R., Barrieu, F., North, G.B., Nobel, P.S., and Chrispeels, M.J. (2002). Plasma membrane aquaporins play a significant role during recovery from water deficit. Plant Physiol. **130:** 2101–2110.

Matsuoka, S., Shibata, T., and Ueda, M. (2009). Statistical analysis of lateral diffusion and multistate kinetics in single-molecule imaging. Biophys. J. **97:** 1115–1124.

Maurel, C., Santoni, V., Luu, D.T., Wudick, M.M., and Verdoucq, L. (2009). The cellular dynamics of plant aquaporin expression and functions. Curr. Opin. Plant Biol. **12:** 690–698.

Maurel, C., Verdoucq, L., Luu, D.T., and Santoni, V. (2008). Plant aquaporins: Membrane channels with multiple integrated functions. Annu. Rev. Plant Biol. **59:** 595–624.

Mayor, S., and Pagano, R.E. (2007). Pathways of clathrin-independent endocytosis. Nat. Rev. Mol. Cell Biol. **8:** 603–612.

Men, S., Boutté, Y., Ikeda, Y., Li, X., Palme, K., Stierhof, Y.D., Hartmann, M.A., Moritz, T., and Grebe, M. (2008). Sterol-dependent endocytosis mediates post-cytokinetic acquisition of PIN2 auxin efflux carrier polarity. Nat. Cell Biol. **10:** 237–244.

Mongrand, S., Morel, J., Laroche, J., Claverol, S., Carde, J.P., Hartmann, M.A., Bonneu, M., Simon-Plas, F., Lessire, R., and Bessoule, J.J. (2004). Lipid rafts in higher plant cells: purification and characterization of Triton X-100-insoluble microdomains from tobacco plasma membrane. J. Biol. Chem. **279:** 36277–36286.

Murphy, A.S., Bandyopadhyay, A., Holstein, S.E., and Peer, W.A. (2005). Endocytotic cycling of PM proteins. Annu. Rev. Plant Biol. **56:** 221–251.

Noda, Y., et al. (2008). Reciprocal interaction with G-actin and tropomyosin is essential for aquaporin-2 trafficking. J. Cell Biol. **182:** 587–601.

Ortiz-Zapater, E., Soriano-Ortega, E., Marcote, M.J., Ortiz-Masiá, D., and Aniento, F. (2006). Trafficking of the human transferrin receptor in plant cells: Effects of tyrphostin A23 and brefeldin A. Plant J. **48:** 757–770.

Otto, B., et al. (2010). Aquaporin tetramer composition modifies the function of tobacco aquaporins. J. Biol. Chem. **285:** 31253–31260.

Pérez-Gómez, J., and Moore, I. (2007). Plant endocytosis: It is clathrin after all. Curr. Biol. **17:** R217–R219.

Pinaud, F., Michalet, X., Iyer, G., Margeat, E., Moore, H.P., and Weiss, S. (2009). Dynamic partitioning of a glycosyl-phosphatidylinositol-anchored protein in glycosphingolipid-rich microdomains imaged by single-quantum dot tracking. Traffic **10:** 691–712.

Postaire, O., Tournaire-Roux, C., Grondin, A., Boursiac, Y., Morillon, R., Schäffner, A.R., and Maurel, C. (2010). A PIP1 aquaporin contributes to hydrostatic pressure-induced water transport in both the root and rosette of *Arabidopsis*. Plant Physiol. **152:** 1418–1430.

Prak, S., Hem, S., Boudet, J., Viennois, G., Sommerer, N., Rossignol, M., Maurel, C., and Santoni, V. (2008). Multiple phosphorylations in the C-terminal tail of plant plasma membrane aquaporins: role in subcellular trafficking of AtPIP2;1 in response to salt stress. Mol. Cell. Proteomics **7:** 1019–1030.

Raffaele, S., et al. (2009). Remorin, a solanaceae protein resident in membrane rafts and plasmodesmata, impairs *potato virus X* movement. Plant Cell **21:** 1541–1555.

Rajan, S.S., Liu, H.Y., and Vu, T.Q. (2008). Ligand-bound quantum dot probes for studying the molecular scale dynamics of receptor endocytic trafficking in live cells. ACS Nano **2:** 1153–1166.

Robinson, D.G., Jiang, L., and Schumacher, K. (2008). The endosomal system of plants: Charting new and familiar territories. Plant Physiol. **147:** 1482–1492.

Schneider, A., Rajendran, L., Honsho, M., Gralle, M., Donnert, G., Wouters, F., Hell, S.W., and Simons, M. (2008). Flotillin-dependent clustering of the amyloid precursor protein regulates its endocytosis and amyloidogenic processing in neurons. J. Neurosci. **28:** 2874–2882.

Shinozaki, Y., Sumitomo, K., Tsuda, M., Koizumi, S., Inoue, K., and Torimitsu, K. (2009). Direct observation of ATP-induced conformational changes in single P2X4 receptors. PLoS Biol. **7:** e103.

Siefritz, F., Tyree, M.T., Lovisolo, C., Schubert, A., and Kaldenhoff, R. (2002). PIP1 plasma membrane aquaporins in tobacco: from cellular effects to function in plants. Plant Cell **14:** 869–876.

Sommer, A., Geist, B., Da Ines, O., Gehwolf, R., Schäffner, A.R., and Obermeyer, G. (2008). Ectopic expression of *Arabidopsis thaliana* plasma membrane intrinsic protein 2 aquaporins in lily pollen increases the plasma membrane water permeability of grain but not of tube protoplasts. New Phytol. **180:** 787–797.

Sorieul, M., Santoni, V., Maurel, C., and Luu, D.T. (2011). Mechanisms and effects of retention of over-expressed aquaporin AtPIP2;1 in the endoplasmic reticulum. Traffic **12:** 473–482.

Takano, J., Miwa, K., Yuan, L., von Wirén, N., and Fujiwara, T. (2005). Endocytosis and degradation of BOR1, a boron transporter of *Arabidopsis thaliana*, regulated by boron availability. Proc. Natl. Acad. Sci. USA **102:** 12276–12281.

Törnroth-Horsefield, S., Wang, Y., Hedfalk, K., Johanson, U., Karlsson, M., Tajkhorshid, E., Neutze, R., and Kjellbom, P. (2006). Structural mechanism of plant aquaporin gating. Nature **439:** 688–694.

Ulbrich, M.H., and Isacoff, E.Y. (2007). Subunit counting in membrane-bound proteins. Nat. Methods **4:** 319–321.

Van Wilder, V., Miecielica, U., Degand, H., Derua, R., Waelkens, E., and Chaumont, F. (2008). Maize plasma membrane aquaporins belonging to the PIP1 and PIP2 subgroups are *in vivo* phosphorylated. Plant Cell Physiol. **49:** 1364–1377.

Vera-Estrella, R., Barkla, B.J., Bohnert, H.J., and Pantoja, O. (2004). Novel regulation of aquaporins during osmotic stress. Plant Physiol. **135:** 2318–2329.

Verdoucq, L., Grondin, A., and Maurel, C. (2008). Structure-function analysis of plant aquaporin AtPIP2;1 gating by divalent cations and protons. Biochem. J. **415:** 409–416.

Wang, X., Teng, Y., Wang, Q., Li, X., Sheng, X., Zheng, M., Samaj, J., Baluska, F., and Lin, J. (2006). Imaging of dynamic secretory vesicles in living pollen tubes of *Picea meyeri* using evanescent wave microscopy. Plant Physiol. **141:** 1591–1603.

Xiao, Z., Ma, X., Jiang, Y., Zhao, Z., Lai, B., Liao, J., Yue, J., and Fang, X. (2008). Single-molecule study of lateral mobility of epidermal growth factor receptor 2/HER2 on activation. J. Phys. Chem. B **112:** 4140–4145.

Zelazny, E., Borst, J.W., Muylaert, M., Batoko, H., Hemminga, M.A., and Chaumont, F. (2007). FRET imaging in living maize cells reveals that plasma membrane aquaporins interact to regulate their subcellular localization. Proc. Natl. Acad. Sci. USA **104:** 12359–12364.

Zhang, D., Manna, M., Wohland, T., and Kraut, R. (2009a). Alternate raft pathways cooperate to mediate slow diffusion and efficient uptake of a sphingolipid tracer to degradative and recycling compartments. J. Cell Sci. **122:** 3715–3728.

Zhang, Q., Li, Y., and Tsien, R.W. (2009b). The dynamic control of kiss-and-run and vesicular reuse probed with single nanoparticles. Science **323:** 1448–1453.

Zhang, W., Jiang, Y., Wang, Q., Ma, X., Xiao, Z., Zuo, W., Fang, X., and Chen, Y.G. (2009c). Single-molecule imaging reveals transforming growth factor-β-induced type II receptor dimerization. Proc. Natl. Acad. Sci. USA **106:** 15679–15683.